

Quantum cascade laser frequency combs

Final Project Report for the Marshall Plan Scholarship Program

Contractor: Nikola Opačak

Postdoctoral researcher, TU Wien
Institute of Solid State Electronics E362
Gußhausstraße 25-25a, A-1040 Wien
Phone: +43 1 58801 362 15
E-Mail: nikola.opacak@tuwien.ac.at

Supervisor at TU Wien:
Prof. Benedikt Schwarz
TU Wien
Institute of Solid State Electronics E362
Gußhausstraße 25-25a, A-1040 Wien
Phone: +43 1 58801 362 14
E-Mail: benedikt.schwarz@tuwien.ac.at

Supervisor at Harvard University:
Prof. Federico Capasso
Harvard University
School of Engineering and Applied Sciences
29 Oxford Street, Cambridge MA 02138
Phone: (617) 384-7611
E-Mail: capasso@seas.harvard.edu

Contents

1	Introduction: Scientific Context of the Conducted Research	2
1.1	Choice of the laser geometry	3
2	Task 1 – Theoretical model and numerical simulations	4
2.1	Maxwell-Bloch system of equations	4
2.2	Inclusion of the linewidth enhancement factor (LEF)	7
2.3	Master equation	10
2.4	Complex Ginzburg-Landau theory of ring QCLs	12
2.5	Dark solitons in ring QCLs – Nozaki-Bekki holes of the CGLE	16
2.5.1	Numerical results	17
3	Task 2 – Device characterization and experimental measurements	20
3.1	Ring QCL device	21
3.2	Frequency comb and dark soliton characterization	22
4	Conclusion and impact of the conducted research	27
5	References	28

1 Introduction: Scientific Context of the Conducted Research

Optical frequency combs are perfectly periodic waveforms of light whose optical spectra consists of a large number of modes with an equal frequency spacing between them – akin to the teeth of an extremely precise comb. Precision been has ever since at the heart of optical frequency combs and it is the main driving force behind their development [1]. Presently, optical frequency combs remain as one of the keystones of optics and have an enormous influence on modern society with uses ranging from fundamental science and astrophysics to precise ranging, communication, frequency metrology, and spectroscopy [2–4]. The latter is the main motivator behind this project.

Spectroscopic applications often utilize coherent light sources especially in the mid-infrared spectral region, as many molecules have their roto-vibrational transitions exactly there and no other spectral region provides the same sensitivity and selectivity for probing various chemical traces. With this in mind, it is clear why the generation of broadband optical combs in the mid-infrared represents a highly-coveted goal. Traditional state-of-the-art solutions for the mid-infrared photonics often rely on expensive and bulky components with dimensions on the scale of an optical table. An alternative that is gaining progressively more attention is the use of semiconductor laser platforms which allow measurements of molecular fingerprints within a millisecond acquisition time freed of the need for any movable parts, thus enabling a higher level of miniaturization and integration.

Quantum cascade laser (QCL) [5] represents the dominant semiconductor laser source in the mid-infrared region with output powers that exceed the Watt level at room temperature conditions. In contrast to most semiconductor lasers, which utilize interband optical transitions and the recombination of electrons and holes to emit photons, QCLs are intersubband unipolar devices. The carrier population inversion that provides the necessary optical gain is achieved within the conduction band and the photon emission occurs via cascading of electrons through periodic potentials in the active region of the laser that comprise large number of different thin semiconductor layers [6]. The intersubband nature of the optical gain bestows QCLs with some unique properties. First of all, the transition wavelegth can be tailored almost at will purely through a change of the confining potential by modifying the semiconductor layers thicknesses and material composition. This is a highly desirable characteristic compared to the case of interband lasers, where the transition wavelength is restricted to the value of the energy bandgap of the utilized semiconductor material. Secondly, intersubband carrier transitions are dominated by intersubband scattering, which happens on the subpicosend time scale. This yields ultrafast gain recovery times of QCLs, compared to the gain recovery times of other semiconductor lasers that lie in the nanosecond range. The ultrafast gain dynamics is responsible for a giant resonant third-order optical nonlinearity [7] that these lasers posses, which can exceed the bulk crystalline nonlinearity of the constituent materials by several orders of magnitude – thus putting QCLs upfront as an ideal test bed for the investigation of nonlinear optics phenomena.

Yet another highly attractive characteristic of QCLs is that they are able to form free-running optical frequency combs without the need of any additional optical components [8], which enabled the first realization of a compact and electrically-driven frequency-comb platform in the mid-infrared. This unique and mesmerising ability to spontaneously emit stable frequency comb waveforms is greatly owed exactly to the giant resonant third-order nonlinearity of QCLs [7, 9]. In the following few years, research on self-starting frequency combs in semiconductor lasers and especially in

QCLs has boomed, with reports on frequency-modulated combs in Fabry-Perot laser cavities [9–11], actively mode-locked combs that emit short pulses [12], and also self-starting combs in a ring resonator [13]. With the potential applications serving as a powerful driving force, the research about novel ways how to form broadband mid-infrared combs in QCLs remains intense.

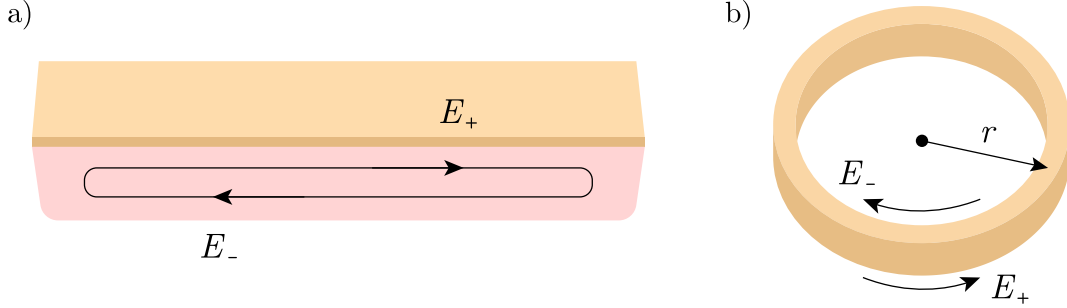


Figure 1: Possible semiconductor laser geometries. **a)** In a Fabry-Perot resonator, the electrical field propagates in both directions due to reflections at the cavity facets, as is illustrated by the counter-propagating field components E_{\pm} . **b)** In an ideal ring laser resonator, the field is unidirectional and is propagating either in a clockwise or counterclockwise direction.

1.1 Choice of the laser geometry

Out of the two possible laser resonator geometries, the Fabry-Perot and the ring resonator, we have identified the latter as being highly attractive for investigating novel frequency comb physics early within the execution of the workplan of this project. The motivation behind this is manifold. First of all, the underlying phys

$$\begin{aligned}
 E(z, t) &= \frac{1}{2} [E_+(z, t)e^{i(\omega_0 t - k_0 z)} + E_-(z, t)e^{i(\omega_0 t + k_0 z)} + \text{c.c.}], \\
 n_{ul}(z, t) &= \sigma_+(t)e^{i(\omega_0 t - k_0 z)} + \sigma_-(t)e^{i(\omega_0 t + k_0 z)}, \\
 n_l(z, t) &= n_{l0}(t) + n_{l2}(t)e^{-2ik_0 z} + n_{l2}^*(t)e^{2ik_0 z}, \\
 n_u(z, t) &= n_{u0}(t) + n_{u2}(t)e^{-2ik_0 z} + n_{u2}^*(t)e^{2ik_0 z}.
 \end{aligned} \tag{1}$$

ical mechanism behind the multimode emission – a prerequisite of frequency comb operation – is fundamentally different in Fabry-Perot and ring lasers. In the former, the multimode optical spectrum stems from the fact that the laser field inside the cavity propagates in both directions due to the reflection at the cavity facets, as is seen in Fig. 1a). Due to this bidirectionality, a standing wave pattern of the intensity is formed inside the laser cavity, where the intensity is weaker at the nodes and stronger at the anti-nodes. Consequently, due to gain saturation, the carrier population inversion is almost bleached out by the higher number of photons at the anti-nodes, and conversely, almost left untouched at the position of the nodes. A different laser cavity longitudinal mode might produce a standing wave pattern which has a better spatial overlap with the untapped excess of optical gain at the nodes, which means that it would get amplified and start to lase as well. This phenomenon is known as spatial hole burning and is the main reason behind multimode laser emission in Fabry-Perot resonators [9].

In a ring laser cavity, where there are no intracavity points of reflection that break the rotational symmetry, the laser field is unidirectional and it propagates in either clockwise or counterclockwise direction [14], as is seen in Fig. 1b). This means that the spatial hole burning is nonexistent in a ring resonator and the multimode laser emission, which is experimentally observed [13, 15], needs to be accounted for in a different way. This still largely represents uncharted territory and it is the main reason why we have opted to investigate ring QCLs at the beginning of this project. As will be seen in description of the theoretical framework, the nuanced interplay of dispersive and nonlinear effects in a ring laser enables not only a variety of intensity waveforms and multimode emission, but also stable frequency comb emission.

The spatial hole burning, caused by a strong single mode that propagates inside the Fabry-Perot laser cavity, provides a Lorentzian-shaped optical gain for the other other longitudinal modes, thus allowing them to overcome the lasing threshold [16]. Its presence in Fabry-Perot cavities overpowers any kind of additional parametric gain that originates from the interplay between the dispersion and nonlinearity, thus preventing us to explore the rich nonlinear dynamics that can lead to novel frequency comb physics. In order to mitigate this effect, our resonator of choice remained to be the ring resonator for the entirety of the project.

2 Task 1 – Theoretical model and numerical simulations

Within the Task 1 of this project, we have successfully developed a sophisticated theoretical model of a semiconductor laser and applied it to a ring QCL. Within this section, we begin with the standard theoretical considerations of the current state-of-art description, and then significantly expand it in order to include several physical phenomenons that are crucial for frequency comb dynamics. Some of the considerations have been published as sections of my doctoral thesis after the end of this research project [17].

2.1 Maxwell-Bloch system of equations

The interaction between the electromagnetic radiation and matter is conveniently described with the optical complex susceptibility, which is defined through a density-matrix formalism χ [18]. the resulting set of equations, which are often referred to as the Maxwell-Bloch equations, represent the state-of-the art in modeling the coherent spatio-temporal evolution of light inside any medium – including the laser cavity and active region.

The laser model is based on a system consisting of three levels, as is depicted on Fig. 2. The lasing transition occurs between the upper and lower laser level, here denoted with u and l , respectively. An additional ground level g describes the depopulation of the other two levels through various scattering channels. dephasing

The Hamiltonian of the system can be represented as $\hat{H} = \hat{H}_0 + \hat{H}'$, where the interaction between the two levels and the electric field is described with $\hat{H}' = -\hat{\mu}E(t)$, where $\hat{\mu}$ is the dipole moment operator. The unperturbed Hamiltonian \hat{H}_0 is defined as

$$\hat{H}_0 = \begin{bmatrix} W_l & 0 \\ 0 & W_u \end{bmatrix} = \begin{bmatrix} \hbar\omega_l & 0 \\ 0 & \hbar\omega_u \end{bmatrix}, \quad (2)$$

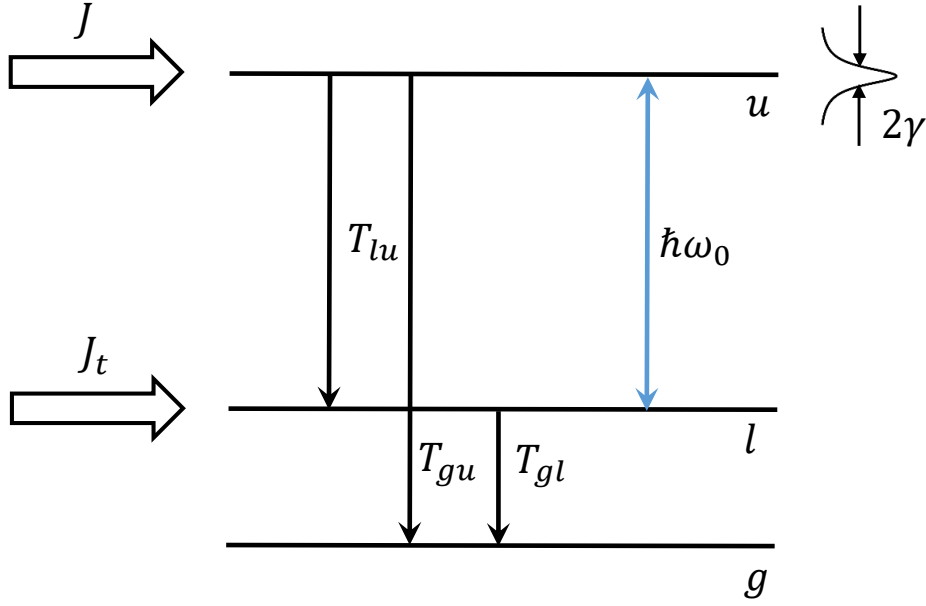


Figure 2: Laser system modeled as an open two-level system described with the Bloch equations. The upper and the lower lasing level are denoted with u and l , and g represents the ground level. Nonradiative transition lifetimes from level i to level j are denoted with T_{ji} . The optical transition linewidth is given with $2\gamma = 2/T_2$, where T_2 is the dephasing time which describes the decay of the transition coherence. The current J represents the pumping rate of the carriers to the upper level, and J_t models the thermal excitation of carriers to the lower lasing level. the currents are normalized to the elementary charge.

where $W_{u,l} = \hbar\omega_{u,l}$ are the energies of the corresponding states u, l . The perturbation Hamiltonian \hat{H}' is given with

$$\hat{H}' = \begin{bmatrix} 0 & -\mu_{lu}E \\ -\mu_{ul}E & 0 \end{bmatrix} \quad (3)$$

where the diagonal elements of the dipole moment operator¹ $\hat{\mu}$ are zero due to the symmetry considerations, assuming that the wavefunctions assigned to the states u and l have a definite parity. Furthermore, we will consider that the dipole matrix element of the lasing transition fulfills $\mu_{ul} = \mu_{lu} = \mu$.

The time evolution of the density matrix $\hat{\rho}$ is governed by the von Neumann equation, which we now write for the time flow in direction $\propto \exp(+i\omega t)$

$$\begin{aligned} \frac{d\hat{\rho}}{dt} &= \frac{i}{\hbar}[\hat{H}, \hat{\rho}] = i \begin{bmatrix} \omega_l & -\frac{\mu E}{\hbar} \\ -\frac{\mu E}{\hbar} & \omega_u \end{bmatrix} \begin{bmatrix} \rho_{ll} & \rho_{lu} \\ \rho_{ul} & \rho_{uu} \end{bmatrix} - i \begin{bmatrix} \rho_{ll} & \rho_{lu} \\ \rho_{ul} & \rho_{uu} \end{bmatrix} \begin{bmatrix} \omega_l & -\frac{\mu E}{\hbar} \\ -\frac{\mu E}{\hbar} & \omega_u \end{bmatrix} \\ &= i \begin{bmatrix} -\frac{\mu E}{\hbar}(\rho_{ul} - \rho_{lu}) & -\rho_{lu}(\omega_u - \omega_l) - \frac{\mu E}{\hbar}(\rho_{uu} - \rho_{ll}) \\ \rho_{lu}(\omega_u - \omega_l) + \frac{\mu E}{\hbar}(\rho_{uu} - \rho_{ll}) & \frac{\mu E}{\hbar}(\rho_{ul} - \rho_{lu}) \end{bmatrix}, \end{aligned} \quad (4)$$

while bearing in mind that $\rho_{lu} = \rho_{ul}^*$ is valid. In order to simplify the notation, the resonant transition frequency ω_0 is introduced as $\omega_0 = \omega_u - \omega_l$. Additional renormalization of the variables is considered in order to give them an appropriate physical meaning. Since the diagonal elements $\rho_{ll,uu}$ represent

¹The dipole moment operator is found as $\hat{\mu} = -e\hat{x}$, where x the Cartesian axis in the growth direction in case of the QCL. Later, the z -axis is reserved for the direction of light propagation.

occupation probabilities of the levels, we obtain equations for the surface densities n_l and n_u of the levels by multiplying $\rho_{ll,uu}$ with the total sheet carrier density n_{tot} . In the same way, the off-diagonal element is renormalized to $n_{ul} = \rho_{ul}n_{tot}$.

Relaxation processes that lead to the decay of the level populations or the decay of the coherence between the levels are added conveniently to the von Neumann equation in a phenomenological way via decay rates described with the lifetimes as is explained in Fig. 1. The coherence lifetime is defined as $T_2 = 1/\gamma$, where γ is the dephasing rate, and nonradiative transition lifetimes between the levels are added. Additionally, the spatial diffusion of carriers is phenomenologically introduced via the diffusion coefficient D . The pumping current J to the upper level models the carrier injection to achieve population inversion. The thermal excitation of the lower level is modeled with a current J_t to describe the thermal equilibrium population. Both currents are normalized to the elementary charge $J \rightarrow J/e$. The set of equations, known as the Bloch equations, is obtained

$$\begin{aligned}\frac{\partial n_l}{\partial t} &= J_t + \frac{n_u}{T_{lu}} - \frac{n_l}{T_{gl}} + 2\frac{\mu E}{\hbar} \text{Im}(n_{ul}) + D\frac{\partial^2 n_l}{\partial z^2}, \\ \frac{\partial n_u}{\partial t} &= J - n_u\left(\frac{1}{T_{lu}} + \frac{1}{T_{gu}}\right) - 2\frac{\mu E}{\hbar} \text{Im}(n_{ul}) + D\frac{\partial^2 n_u}{\partial z^2}, \\ \frac{\partial n_{ul}}{\partial t} &= \left(i\omega_0 - \frac{1}{T_2}\right)n_{ul} + i\frac{\mu E}{\hbar}(n_u - n_l),\end{aligned}\tag{5}$$

where T_{ji} represents a nonradiative transition lifetime from level i to level j .

The induced macroscopic polarization P , which defines also the optical susceptibility χ , is found to be

$$P = \frac{n_{tot}}{L_p} \text{tr}(\hat{\rho}\hat{\mu}) = \frac{\mu}{L_p}(n_{ul} + n_{ul}^*).\tag{6}$$

Here, L_p is the appropriate dimension of the lasing structure so that n_{tot}/L_p gives the density of carriers. In the case of a QCL, L_p is the period length. The one-dimensional wave equation derived from the Maxwell equations is

$$\frac{\partial^2 E(z, t)}{\partial z^2} - \frac{n_r^2}{c^2} \frac{\partial^2 E(z, t)}{\partial t^2} = \frac{1}{\varepsilon_0 c^2} \frac{\partial^2 P(z, t)}{\partial t^2},\tag{7}$$

where n_r is the refractive index of the bulk material, with a strictly real value $n_r \in \mathbb{R}$. Combining the previous two equations results in

$$\frac{\partial^2 E}{\partial z^2} - \frac{n_r^2}{c^2} \frac{\partial^2 E}{\partial t^2} = \frac{\Gamma\mu}{\varepsilon_0 c^2 L_p} \frac{\partial^2}{\partial t^2} (n_{ul} + n_{ul}^*),\tag{8}$$

where Γ is the confinement factor that describes what portion of the laser light found within the laser cavity. Equation (8) together with (5) constitutes the state-of-the-art Maxwell-Bloch system of equations.

We can make now the so-called slowly varying envelope approximation and write the ansatz that separates the physical values into a fast-oscillating carrier wave and a slowly-varying envelope

function

$$\begin{aligned}
E(z, t) &\rightarrow \frac{1}{2}[E(z, t)e^{i(\omega_0 t - k_0 z)} + \text{c.c.}], \\
n_{ul}(z, t) &\rightarrow \sigma(t)e^{i(\omega_0 t - k_0 z)}, \\
n_l(z, t) &\rightarrow n_{l0}(t), \\
n_u(z, t) &\rightarrow n_{u0}(t),
\end{aligned} \tag{9}$$

while bearing in mind the ring resonator geometry and assuming that the electric field is unidirectional. In the equation above, the carrier frequency has the wavenumber $k_0 = n(\omega_0)\omega_0/c$. Substitution of relations (9) into the optical Bloch equations (5) and the wave equation (8) yields the equations for the envelope functions. In the derivation, the rotating-wave approximation is often used, where only the slowly rotating terms, proportional to $\propto \exp(i\omega_0 t)$, are kept. Additionally, the absorption coefficient α_w is added to the wave equations in order to describe the waveguide losses. We obtain

$$\frac{\partial n_{l0}}{\partial t} = J_t + \frac{n_{u0}}{T_{lu}} - \frac{n_{l0}}{T_{gl}} - \frac{\mu}{\hbar} \text{Im}(E\sigma^*), \tag{10}$$

$$\frac{\partial n_{u0}}{\partial t} = J - \left(\frac{1}{T_{lu}} + \frac{1}{T_{gu}}\right)n_{u0} + \frac{\mu}{\hbar} \text{Im}(E\sigma^*), \tag{11}$$

$$\frac{\partial \sigma}{\partial t} = -\frac{\sigma}{T_2} + i\frac{\mu}{2\hbar}E(n_{u0} - n_{l0}), \tag{12}$$

$$\left(\frac{n_r}{c} \frac{\partial}{\partial t} + \frac{\partial}{\partial z}\right)E = -i\frac{\Gamma\mu\omega_0}{n_r\epsilon_0 c L_p}\sigma + i\beta|E|^2E + i\frac{k''}{2}\frac{\partial^2 E}{\partial t^2} - \frac{\alpha_w}{2}E. \tag{13}$$

In the wave equation (13), we have additionally included the absorption coefficient α_w in order to describe the waveguide losses, the bulk crystalline Kerr nonlinearity modeled as a phase variation through the Kerr coefficient β , and a finite group velocity dispersion (GVD), proportional to the coefficient k'' . The latter describes only the GVD contribution from the waveguide (the dispersion from the gain is captured within the polarization variable σ). In actual physical laser systems, the presence of nonvanishing GVD has a profound impact on the intermodal interaction and its absolutely necessary to include it correctly in the model [9, 19].

2.2 Inclusion of the linewidth enhancement factor (LEF)

Semiconductor lasers are set apart from other laser types by numerous unique traits, most of which are attributed to the unique asymmetric shape of the gain spectrum. This has a profound impact on the laser dynamics as well as frequency comb formation, and is most succinctly and successfully encompassed with the so-called linewidth enhancement factor (LEF) [20].

Following the Kramers–Kronig relations, an asymmetric gain shape results in a dispersion curve of the refractive index that has a non-zero value at the gain peak [21]. As a consequence, a remarkable property of semiconductor lasers is that both the refractive index and the optical gain change simultaneously with the varying carrier population. This property was quantified with the linewidth enhancement factor (LEF), also called the α -factor, defined by Charles Henry as the ratio of changes of the modal index and gain [20], which are proportional to the real and imaginary part

of the optical susceptibility (LEF) [20]

$$\alpha(\omega) = -\frac{\partial\chi_R(\omega)/\partial N}{\partial\chi_I(\omega)/\partial N}. \quad (14)$$

Many unique properties of semiconductor lasers can be traced back to the non-zero value of this factor at the gain peak. The LEF was first introduced in the 1980s to describe the broadening of the semiconductor laser linewidth beyond the fundamental Schawlow–Townes limit. Furthermore, the LEF determines the dynamics of semiconductor lasers, as it describes the coupling between the amplitude and the phase of the optical field [22]. In lasers with fast gain recovery times, the LEF was recently connected to the onset of a giant Kerr nonlinearity [7] and frequency modulated combs [9]. It was shown that the light amplitude–phase coupling, quantified by the LEF, can lead to a low-threshold multimode instability and frequency comb formation [13]. Appropriate values of the LEF were predicted to result in the emission of solitons in active media [23]. Precise knowledge of the LEF represents a key point in understanding many astonishing features of semiconductor lasers and subsequently controlling them – making it absolutely crucial to include it properly in the theoretical cavity model in order to study the spatio-temporal evolution of the laser field [24]. This was conducted within the scope of this project and subsequently published in my doctoral dissertation [17].

In order to obtain the expression for the complex optical susceptibility, one starts from the Fourier transform of the differential equation (5) for the off-diagonal density matrix element n_{ul}

$$n_{ul}(\omega) = \frac{\mu}{\hbar} \frac{n_u - n_l}{\omega - \omega_0 - i\gamma} E(\omega), \quad (15)$$

and combine it with the relation $P = \varepsilon_0\chi = \mu n_{ul}/L_p$, which yields

$$\chi(\omega) = \frac{\mu^2}{\varepsilon_0\hbar L_p} \frac{n_u - n_l}{\omega - \omega_0 - i\gamma}. \quad (16)$$

The susceptibility described above defines the optical gain as $g = -\omega\chi_I/n_r c$, which has a symmetric Lorentzian shape characteristic to a transition between atomic levels. The inclusion of gain asymmetry via the LEF can be done in the following way [17]

$$\chi(\omega) = \frac{\mu^2(N_u - N_l)}{\varepsilon_0\hbar} \frac{(1 + i\tilde{\alpha})^2}{\omega - \omega_0 - i\gamma}, \quad (17)$$

where $\tilde{\alpha}$ stands for the value of the LEF at the position of the gain peak given by $\omega_p = \omega_0 + \tilde{\alpha}/T_2$.

Remarkably, inclusion of the LEF at the gain peak $\tilde{\alpha}$ allows to encapsulate the entire spectral behavior of the complex optical susceptibility χ . This can be seen in Fig. 3 for three values of $\tilde{\alpha} = 0, 0.5, \text{ and } 1$. The bottom row of the figure furthermore shows the spectrally resolved $\alpha(\omega)$. The case of a symmetric Lorentzian gain profile corresponds to $\tilde{\alpha} = 0$. Due to Kramers-Kronig relations, the zero-crossing of the real part of the susceptibility is at the gain peak $\chi_R(\omega_p) = 0$, which yields $\alpha(\omega_p) = 0$. Since the lasing wavelength is in the vicinity of the gain peak, carrier induced gain changes will not affect the refractive index that the laser feels in this case. As a result, the amplitude and the phase of the electric field are not coupled and this reflects the situation in solid-state and gas lasers, where the value of LEF is zero. However, if the lasing frequency would

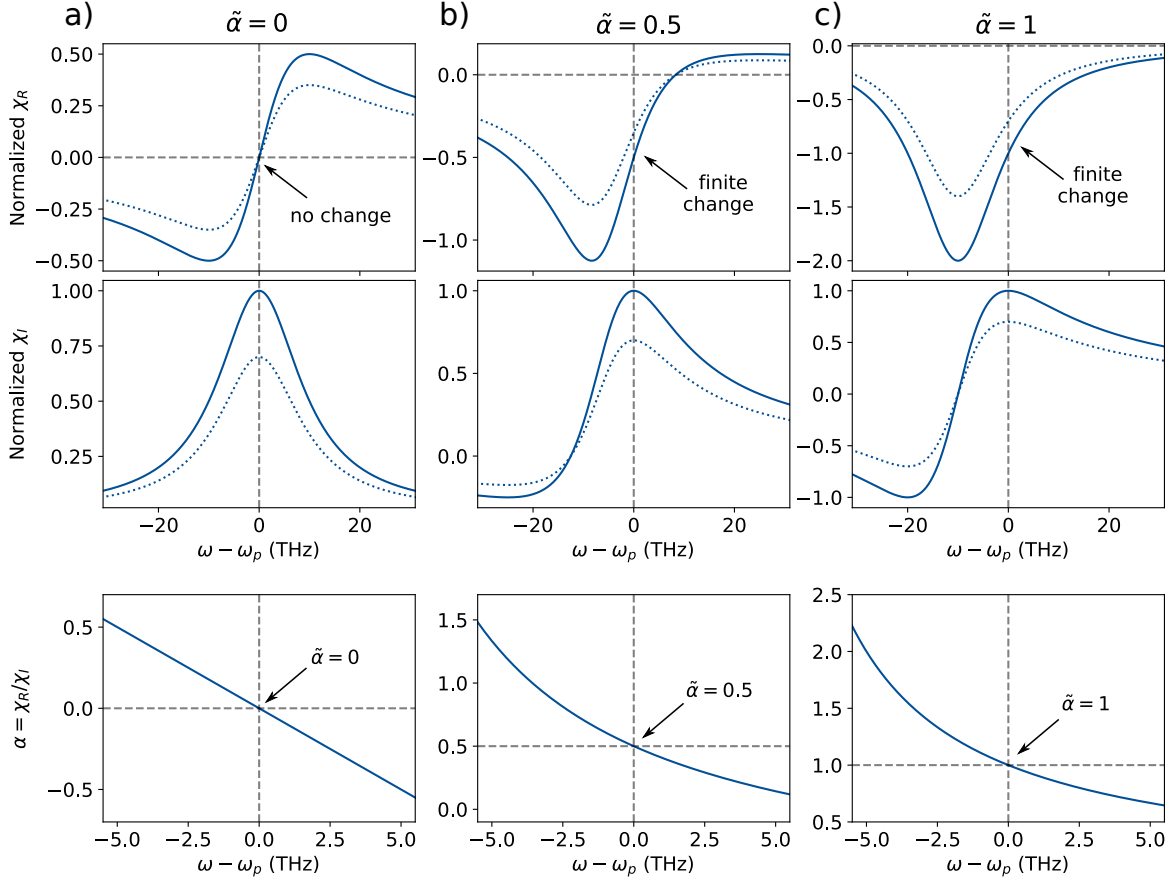


Figure 3: Real χ_R and imaginary χ_I part of the susceptibility, along with the calculated LEF. The susceptibility is defined with equation (17) and is calculated for three values of the LEF at the gain peak: **a)** $\tilde{\alpha} = 0$, **b)** $\tilde{\alpha} = 0.5$, and **c)** $\tilde{\alpha} = 1$. The profile of χ_I becomes more asymmetric with the increasing $\tilde{\alpha}$ and values of χ_R at the gain peak become non-zero and significant. Vertical dashed lines represent the position of the gain peak. Change in the carrier population induces variation of both the χ_R and χ_I (blue dotted lines). For symmetric gainshapes ($\tilde{\alpha} = 0$), χ_R remains zero at the gain peak. On the other hand, changes of χ_R at the gain peak progressively grow for increasing gain asymmetry (growing $\tilde{\alpha}$). In addition to that, the gainwidth broadens for larger $\tilde{\alpha}$. T_2 is set to 100 fs.

hypothetically be strongly shifted from the gain peak, a strong amplitude-phase coupling would appear, which is reflected by nonzero values of α when detuned from ω_p in Fig. 3a). The sign of the LEF determines the sign of the gain induced change of the refractive index, and it depends on the direction of the detuning.

A nonzero value of $\tilde{\alpha}$ yields an asymmetric shape of the gain, with the increasing asymmetry for larger $\tilde{\alpha}$ (Figs. 3b) and c)). One impact of this dependence reflects in the increasing gainwidth. Furthermore, the zero-crossing of χ_R becomes greatly detuned from ω_p . As a result, the refractive index at the lasing wavelength changes with the varying optical gain, which induces strong amplitude-phase coupling. For increasing gain asymmetry (growing $\tilde{\alpha}$), the change of χ_R at the gain peak increases as well. This is additionally indicated with the larger values of $\alpha(\omega)$. To ensure consistency, one can easily check that $\alpha(\omega_p) = \tilde{\alpha}$ in the bottom row on Fig. 3.

Although growing values of $\tilde{\alpha}$ correspond to the progressively more asymmetric gainshapes, the differences among the gain values are not that large within a narrow range around ω_p where the laser operates. Far larger impact on the multimode dynamics comes from the value of χ_R which

becomes greatly shifted from zero.

We can now include the LEF, and the amplitude-phase coupling it describes, also in the time domain by altering the Maxwell-Bloch equations (10)-(13). Starting from the susceptibility that includes $\tilde{\alpha}$ in equation (17), we arrive at the modified equation for n_{ul} in the time domain [17]

$$\frac{\partial n_{ul}}{\partial t} = \left(i\omega_0 - \frac{1}{T_2}\right)n_{ul} + i\frac{\mu E}{\hbar}(1 + i\tilde{\alpha})^2(n_u - n_l). \quad (18)$$

The LEF affects only the equation for the off-diagonal matrix element, which determines the polarization. The rest of the Bloch equations (5) and the wave equation (8) remain unchanged. Following a procedure similar to the one described earlier, we can apply the slowly varying envelope approximation and obtain the modified equation for σ

$$\frac{\partial \sigma}{\partial t} = -\frac{1 + i\tilde{\alpha}}{T_2}\sigma + i\frac{\mu}{2\hbar}(1 + i\tilde{\alpha})^2 E(n_{u0} - n_{l0}). \quad (19)$$

Equation (19) together with the equations (10)-(13) represents the state-of-the-art Maxwell-Bloch equations which include the impact of a non-zero LEF at the gain peak. They represent an excellent quantitative tool to determine the spatio-temporal evolution of the laser field inside the cavity. However, the full system of Maxwell-Bloch equations is not helpful at gaining any kind of intuitive insight into the governing physics, as a change of one parameter influences the whole system of coupled differential equations. Furthermore, the numerical implementation of such a system can be quite demanding – both for the numerical stability and the costs in terms of the execution time. For this reason, we seek to simplify the governing system of equations by eliminating every variable except the complex electric field envelope E and obtain single master equation that explains the laser dynamics.

2.3 Master equation

In order to derive a master equation [17], we can replace the carrier inversion $n_u - n_l$ by one term denoted with n_0 , which is done formally by neglecting the population of the lower level. We can then turn to the polarization σ in the equation (19) and apply the Fourier transform. Bearing in mind that σ is the slowly varying envelope, and that the carrier frequency is ω_p , we have $\mathcal{F}(\partial^m/\partial t^m) = (i(\omega - \omega_p))^m$, and (19) transforms to

$$\sigma = i\frac{\mu T_2}{2\hbar}(1 + i\tilde{\alpha})^2 \frac{1}{1 + i(\omega - \omega_0)T_2} \mathcal{F}(En_0). \quad (20)$$

In order to eliminate the differential equation for σ , a transfer function $h(\omega) = i(1 + i(\omega - \omega_0))^{-1}$ is introduced and approximated with a Taylor series around the gain peak frequency $\omega_p = \omega_0 + \tilde{\alpha}/T_2$. Terms up to the second order are kept

$$\begin{aligned} h(\omega) &= h(\omega_p) + h'|_{\omega=\omega_p}(\omega - \omega_p) + \frac{1}{2}h''|_{\omega=\omega_p}(\omega - \omega_p)^2 \\ &= \frac{i}{1 + i\tilde{\alpha}} + \frac{T_2}{(1 + i\tilde{\alpha})^2}(\omega - \omega_p) - i\frac{T_2^2}{(1 + i\tilde{\alpha})^3}(\omega - \omega_p)^2. \end{aligned} \quad (21)$$

Bearing in mind that $\sigma(\omega) = \mu T_2 \hbar(\omega) \mathcal{F}(En_0)/(2\hbar)$, equation (20) transforms to

$$\sigma = i \frac{\mu T_2}{2\hbar} (1 + i\tilde{\alpha}) \left[1 - i\tilde{T}_2(\omega - \omega_p) - \tilde{T}_2^2(\omega - \omega_p)^2 \right] \mathcal{F}(En_0), \quad (22)$$

where

$$\tilde{T}_2 = \frac{T_2}{1 + i\tilde{\alpha}} \quad (23)$$

was introduced for conciseness. As the next step, the inverse Fourier transform of (22) can be applied, yielding the expression of the coherence term σ

$$\sigma = i \frac{\mu T_2}{2\hbar} n_0 (1 + i\tilde{\alpha}) \left[E - \tilde{T}_2 \frac{\partial E}{\partial t} + \tilde{T}_2^2 \frac{\partial^2 E}{\partial t^2} \right]. \quad (24)$$

In the case when the gain recovery time is much smaller than the cavity roundtrip time – as is the case for a QCL – the differential equation for the carrier population can be eliminated as well. The lifetime T_1 is introduced as

$$T_1 = \left(\frac{1}{T_{lu}} + \frac{1}{T_{gu}} \right)^{-1}, \quad (25)$$

and we can write the differential equation for the population n_0 as

$$\frac{\partial n_0}{\partial t} = J - \frac{n_0}{T_1} + \frac{\mu}{\hbar} \text{Im}(E\sigma^*). \quad (26)$$

Subsequently, adiabatic elimination of σ from equation (19)

$$\sigma = i \frac{\mu T_2}{2\hbar} E n_0 (1 + i\tilde{\alpha}), \quad (27)$$

which corresponds to the zeroth order in the Taylor series (21), is replaced in the equation for the population n_0 (26)

$$\frac{\partial n_0}{\partial t} = J - \frac{n_0}{T_1} - \frac{\mu^2 T_2}{2\hbar^2} n_0 |E|^2 = J - \frac{n_0}{T_1} \left(1 + \frac{|E|^2}{I_s} \right), \quad (28)$$

The value of n_0 is real and does not have a direct impact on the phases of the field envelope. Hence, we expect that calculating the adiabatic approximation by setting the time derivatives to zero in the equation (28) would be sufficient [9]. We obtain

$$n_0 = \frac{T_1 J}{1 + \frac{|E|^2}{I_s}}. \quad (29)$$

It is now possible to substitute the expression (29) for the population n_0 into the definition of the coherence term σ , given with the relation (24) to obtain

$$\sigma = i \frac{\mu T_1 T_2 J}{2\hbar \left(1 + \frac{|E|^2}{I_s} \right)} (1 + i\tilde{\alpha}) \left[E - \tilde{T}_2 \frac{\partial E}{\partial t} + \tilde{T}_2^2 \frac{\partial^2 E}{\partial t^2} \right]. \quad (30)$$

Finally, inserting equation (30) into the wave equation (13) results in a single laser master equation

$$\begin{aligned} \frac{n_r}{c} \frac{\partial E}{\partial t} + \frac{\partial E}{\partial z} = \frac{g(I)}{2} (1 + i\tilde{\alpha}) \left[E - \tilde{T}_2 \frac{\partial E}{\partial t} + \tilde{T}_2^2 \frac{\partial^2 E}{\partial t^2} \right] \\ - \frac{\alpha_w}{2} E + i\beta |E|^2 E + i \frac{k''}{2} \frac{\partial^2 E}{\partial t^2}, \end{aligned} \quad (31)$$

where the saturated gain $g(I)$ in the units of $1/m$ is introduced as

$$g(I) = \frac{g_0}{1 + \frac{|E|^2}{I_s}} = \frac{g_0}{1 + \frac{I}{I_s}}, \quad (32)$$

and the unsaturated gain coefficient g_0 is defined as

$$g_0 = \frac{\Gamma \mu^2 \omega_0 T_1 T_2 J}{\hbar n_r c \varepsilon_0 L_p}. \quad (33)$$

In this way, the full system of coupled differential Maxwell-Bloch equations is reduced down to a single master equation. It provides an excellent quantitative tool for a laser which possesses fast gain dynamics. However, even if that is not the case, equation (31) is still useful as a qualitative tool to gain insight into the underlying physics. Furthermore, the crucial impact of a non-zero LEF is successfully encapsulated, thus allowing to continue with the investigation.

2.4 Complex Ginzburg-Landau theory of ring QCLs

In order to form an optical frequency comb, mechanisms that trigger lasing modes at different frequencies, and mutually lock their amplitudes and phases, need to be present inside the cavity. This is achieved in various ways depending on the platform for frequency comb generation.

In stark contrast to the Fabry-Perot lasers where the multimode regime is enabled by the spatial hole burning, a ring resonator possesses rotational symmetry (Fig. 1b)) and lacks any reflection points which could couple the opposite-propagating components of the field. This results in unidirectional operation, where either the clockwise or counterclockwise field component lases. Due to unidirectional lasing, the effect of spatial hole burning is not present inside the cavity and the laser is expected to operate in single-mode emission. Surprisingly, a transition to multimode operation was observed in mid-infrared and THz QCLs at an injection level only fractionally higher than the lasing threshold [13, 15, 25, 26]. Moreover, the coherence of the state is manifested by its narrow beatnote, which indicates its frequency comb nature. A notable feature of the instability is that as the current in the device is increased, the laser can revert back to single-mode operation – a feature not observed in regular Fabry-Perot lasers.

The exact mechanisms that lead to multimode operation and potential formation of frequency combs were shown to originate from a wave instability [13] – a process that is known from hydrodynamics [27] and represents a mechanism by which a small disturbance in a wave grows in amplitude owing to nonlinear interactions. The instability condition is set into the framework of the famous complex Ginzburg-Landau formalism [28], where the low-threshold instability occurs due to the phase turbulence – a phenomenon that was previously not connected to photonics in any way.

We will obtain the complex Ginzburg-Landau equation (CGLE) starting from the derived master equation (31). The procedure is published in my doctoral thesis [17], and is similar to the one published in Ref. [13]. In the first step, the term $\tilde{T}_2 \partial E / \partial t$ in the large parenthesis of the right hand side of equation (31) is neglected. This is justified, as its main effect is to introduce a constant shift of the value of the refractive index n_r . Additionally, one needs to bear in mind that the master equation is derived from the Maxwell-Bloch equations that utilize the rotating wave approximation. Therefore, substituting the second time derivative $\partial^2 / \partial t^2$ with the second spatial derivative $(c/n_r)^2 \partial^2 / \partial z^2$ is an excellent approximation. Moreover, the system is switched to a frame of reference that moves together with the propagating field by applying coordinate transformations $z \rightarrow z - \frac{c}{n_r} t$ and $t \rightarrow t$. Equation (31) then transforms to

$$\begin{aligned} \frac{n_r}{c} \frac{\partial E}{\partial t} &= \frac{g(I)}{2} (1 + i\tilde{\alpha}) \left(E + \tilde{T}_2^2 \frac{c^2}{n_r^2} \frac{\partial^2 E}{\partial z^2} \right) \\ &- \frac{\alpha_w}{2} E + i\beta |E|^2 E + i \frac{k''}{2} \frac{c^2}{n_r^2} \frac{\partial^2 E}{\partial z^2}. \end{aligned} \quad (34)$$

It is now of use to write the first order Taylor expansion of the saturated gain $g(I)$ around the stationary intensity $I_0 = I_s (\frac{g_0}{\alpha_w} - 1)$ in the form of

$$g(I) = \frac{g_0}{1 + \frac{I}{I_s}} \approx g(I_0) + \frac{\partial g(I)}{\partial I} \Big|_{I=I_0} (I - I_0) \approx g_1 - g_2 \frac{I}{I_s}. \quad (35)$$

The coefficients g_1 and g_2 are found to be

$$g_1 = \frac{\alpha_w}{g_0} (2g_0 - \alpha_w), \quad g_2 = \frac{\alpha_w^2}{g_0}. \quad (36)$$

Close to the lasing threshold $g_0 \approx \alpha_w$, it holds $g_1 \approx g_2 \approx g_0$.

Combining relations (34), (35) and (36) yields

$$\begin{aligned} \frac{n_r}{c} \frac{\partial E}{\partial t} &= \left(\frac{g_1}{2} - \frac{g_2}{2} \frac{|E|^2}{I_s} \right) (1 + i\tilde{\alpha}) \left(E + \tilde{T}_2^2 \frac{c^2}{n_r^2} \frac{\partial^2 E}{\partial z^2} \right) \\ &- \frac{\alpha_w}{2} E + i\beta |E|^2 E + i \frac{k''}{2} \frac{c^2}{n_r^2} \frac{\partial^2 E}{\partial z^2}. \end{aligned} \quad (37)$$

New functions a_1 , a_2 , a_3 , and a_4 are furthermore introduced for simplicity

$$\begin{aligned} \left(\frac{1}{1 + i\tilde{\alpha}} \right)^2 &= a_1 + ia_2 \\ a_1 &= \frac{1 - \tilde{\alpha}^2}{(1 + \tilde{\alpha}^2)^2} \\ a_2 &= -\frac{2\tilde{\alpha}}{(1 + \tilde{\alpha}^2)^2} \\ a_3 &= a_1 - \tilde{\alpha}a_2 = \frac{1}{1 + \tilde{\alpha}^2} \\ a_4 &= a_2 + \tilde{\alpha}a_1 = -\frac{\tilde{\alpha}}{1 + \tilde{\alpha}^2}. \end{aligned} \quad (38)$$

We can then write

$$(1 + i\tilde{\alpha}) \left[1 + \left(\frac{1}{1 + i\tilde{\alpha}} \right)^2 \right] = 1 + i\tilde{\alpha} + a_3 + ia_4. \quad (39)$$

Combining relations (37), (38), and (39) yields

$$\begin{aligned} \frac{n_r}{c} \frac{\partial E}{\partial t} &= \left(\frac{g_1}{2} - \frac{g_2}{2} \frac{|E|^2}{I_s} \right) \left[1 + i\tilde{\alpha} + (a_3 + ia_4) T_2^2 \frac{c^2}{n_r^2} \frac{\partial^2}{\partial z^2} \right] E \\ &\quad - \frac{\alpha_w}{2} E + i\beta |E|^2 E + i \frac{k''}{2} \frac{c^2}{n_r^2} \frac{\partial^2 E}{\partial z^2}. \end{aligned} \quad (40)$$

Reordering the terms in the equation above and neglecting the term proportional to $\sim |E|^2 \partial^2 E / \partial z^2$ results in equation

$$\frac{\partial E}{\partial t} = (\eta + i\omega_s) E + (d_R + id_I) \frac{\partial^2 E}{\partial z^2} - (n_R + in_I) |E|^2 E, \quad (41)$$

where the following functions have been introduced

$$\begin{aligned} \eta &= \frac{g_1 - \alpha_w}{2} \frac{c}{n_r}, & \omega_s &= \frac{g_1 \tilde{\alpha}}{2} \frac{c}{n_r}, \\ d_R &= \frac{g_1 T_2^2}{2(1 + \tilde{\alpha}^2)} \frac{c^3}{n_r^3}, & d_I &= \left(\frac{k''}{2} - \frac{\tilde{\alpha} g_1 T_2^2}{2(1 + \tilde{\alpha}^2)} \right) \frac{c^3}{n_r^3}, \\ n_R &= \frac{g_2}{2I_s} \frac{c}{n_r}, & n_I &= - \left(\beta - \frac{\tilde{\alpha} g_2}{2I_s} \right) \frac{c}{n_r}. \end{aligned} \quad (42)$$

Here, the laser net gain is described with the coefficient η , and ω_s represents the frequency shift due to the gain asymmetry quantified by $\tilde{\alpha}$ (LEF at the gain peak). The complex diffusion coefficient, given with $d_R + id_I$, dampens variations of the field E . Its complex value can be easily understood as it will work towards smoothing any spatial gradient of both the amplitude and phase. Physically, it emerges from the curvature of the gain (due to its finite bandwidth), asymmetric gain-shape, and the GVD. Lastly, the nonlinearity is described with $n_R + in_I$. The real part n_R arises from the gain saturation in the laser and dampens the amplitude fluctuations. The imaginary part n_I describes the phase modulation and it is due to the Kerr nonlinearity and a finite LEF.

Equation (42) can be written in a more elegant way. To do so, time, spatial variable, and the field need to be rescaled

$$\begin{aligned} t &\rightarrow \frac{t}{\eta}, \\ z &\rightarrow \left(\frac{d_R}{\eta} \right)^{1/2} z \\ E &\rightarrow \left(\frac{\eta}{n_R} \right)^{1/2} e^{i\omega_s t / \eta} E. \end{aligned} \quad (43)$$

Moreover, dispersion and nonlinearity parameters are introduced as c_D and c_{NL} in the following

way

$$\begin{aligned} c_D &= -\tilde{\alpha} + k'' \frac{g_0(1 + \tilde{\alpha}^2)}{\alpha_w(2g_0 - \alpha_w)T_2^2}, \\ c_{NL} &= \tilde{\alpha} - \beta \frac{2I_s g_0}{\alpha_w^2}. \end{aligned} \quad (44)$$

From the previous relation, it is clear how the GVD influences c_D and the Kerr nonlinearity influences c_{NL} , while the LEF influences both of them. Implementing relations (43) and (44) into equation (42) allows for obtaining the conventional form of CGLE often found in literature [28]

$$\frac{\partial E}{\partial t} = E + (1 + ic_D) \frac{\partial^2 E}{\partial z^2} - (1 + ic_{NL}) |E|^2 E. \quad (45)$$

In comparison with the laser master equation (31), the entire parameter space of CGLE has been reduced to just two dimensions defined by the $c_D - c_{NL}$ plane. Once again, it can be observed that the LEF directly impacts both parameters in relation (44).

The CGLE represents one of the most celebrated nonlinear equations in physics. A vast amount of nonlinear phenomena can be described on a qualitative, and often even on a quantitative level, by employing the CGLE. These include nonlinear waves in diverse media, second-order transitions, superconductivity, superfluidity, Bose-Einstein condensation, liquid crystals, and strings in field theory. Realizing this, it should come as no surprise that nonlinear phenomena in fast semiconductor lasers are also governed by the CGLE to some extent [13].

In order to explain the multimode instability, we can perform the linear stability analysis of the CGLE (45), where a small perturbation of a single-mode wave is assumed. If the perturbation grows over time instead of decaying, the single-mode solution is unstable. The analysis yields the Benjamin-Feir-Newell criterion of stability

$$1 + c_D c_{NL} > 0. \quad (46)$$

If the criterion is violated, a band of unstable wavenumbers arises and destabilizes the plane wave solution. In a laser, a competition between multiple different optical modes emerges, resulting in multimode emission. This means that a laser can go past its multimode instability threshold depending only on the values of the parameters such as the GVD, Kerr nonlinearity or the LEF – if $1 + c_D c_{NL} < 0$ holds. No additional effect (e.g. spatial hole burning) is required.

Bearing in mind the stability analysis of the CGLE that yielded the Benjamin-Feir-Newell criterion of stability (46), we can divide the two-dimensional parameter space spun by c_D and c_{NL} into two well defined regions – the stable one, where the laser emits a single-mode, and the unstable region, where multimode emission occurs due to phase and amplitude turbulence (the white and blue regions in Fig. 4). The boundary between the region is defined by the condition $1 + c_D c_{NL} = 0$.

Deep inside the unstable region, when $1 + c_D c_{NL} \ll 0$, we enter the defect turbulence regime characterized by large variations of the intensity. The resulting laser state is broadband and governed by chaos, however it cannot form a stable frequency comb. Moving closer to the border of the unstable region, where $1 + c_D c_{NL} \lesssim 0$, we switch to the phase turbulence regime. Here the intensity variations are smaller, the spectral width is narrower, but the laser can form a periodic

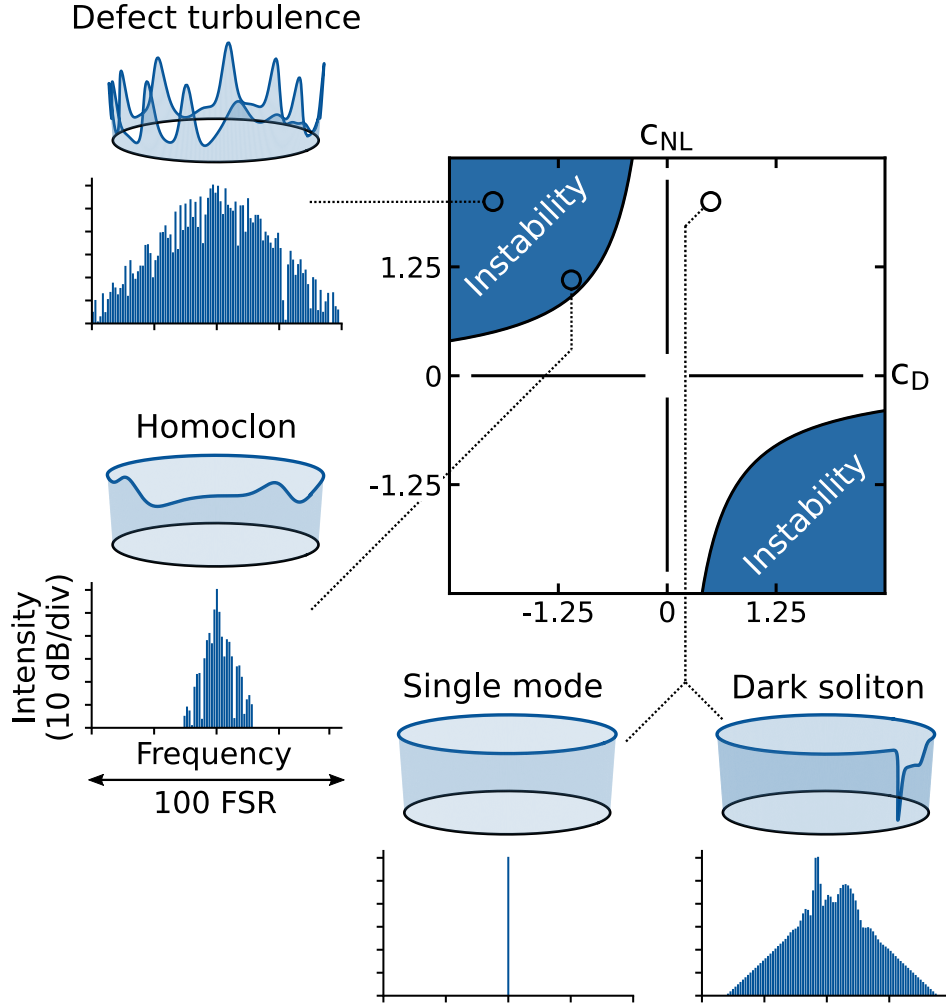


Figure 4: Parameter space of the CGLE spun by c_D and c_{NL} can be divided into the stable (white) region, which supports single-mode laser emission, and the unstable (blue) region, where the laser operates in multimode due to turbulence [13]. The regions are separated by the condition $1 + c_D c_{NL} = 0$. Deep inside the unstable region ($1 + c_D c_{NL} \ll 0$), the laser is in the defect turbulence regime exhibiting large variations of the intensity, and it cannot form a frequency comb. Closer to the stability boundary, the laser undergoes phase turbulence where the intensity variations are smaller, eventually leading to a frequency comb state known as homoclon. Probing a point in the stable region, a stable single-mode operation is observed. However, at the same point, going beyond the linear stability analysis, the laser can undergo a multimode instability, thus forming states known as Nozaki-Bekki holes. They are characterized as dark solitons – dark solitary pulses that connect two plane waves.

waveform and emit a stable frequency comb, as is seen in Fig. 4. These states – known as homoclons – were recently observed in QCL rings [13], thus explaining frequency comb formation in these lasers.

Within this project, we have discovered yet another type of frequency combs that emerge in fast semiconductor ring lasers. The findings are still unpublished.

2.5 Dark solitons in ring QCLs – Nozaki-Bekki holes of the CGLE

If we probe a point of the CGLE parameter space where $1 + c_D c_{NL} > 0$, the single-mode plane wave solution is found to be stable. However, if we go beyond the linear stability analysis and assume the possibility of large perturbations, we can find that a multimode state can coexist with

a stable single-mode wave at the same point in the CGLE parameter space, as can be seen in Fig. 4. This state is known as a Nozakki-Bekki hole (NBH) [29]. The bandwidth of NHBs is similar to the state of defect turbulence, yet it is perfectly periodic and forms a stable frequency comb. The waveform exhibits a dark pulse, surrounded by an otherwise constant intensity, and it can be viewed as a type of a dark soliton. Solitons represent localized, solitary waves that have become vastly popular in photonics in recent years due to the fact that they form a broad equidistant spectrum which can be used in numerous applications [30]. So far, solitons have been reported in optical fibers and microresonators, and are driven by means of an external optical single-mode pump, whereby the numerous sidemodes are excited by the crystalline Kerr nonlinearity. However, both optical fibers and microresonators represent passive media with no optical gain, thus requiring an external optical pump, which significantly raises the complexity of the system. The possibility of emitting solitons from a monolithic, electrically-driven platform, such as a semiconductor laser, is highly appealing and could be a game-changer in the field of integrated sensing.

2.5.1 Numerical results

A systematic parameter sweeps of the master equation (31) has indeed confirmed the existence of the NBHs as well – thus deepening the connection between fast gain media such as QCLs and the CGLE.

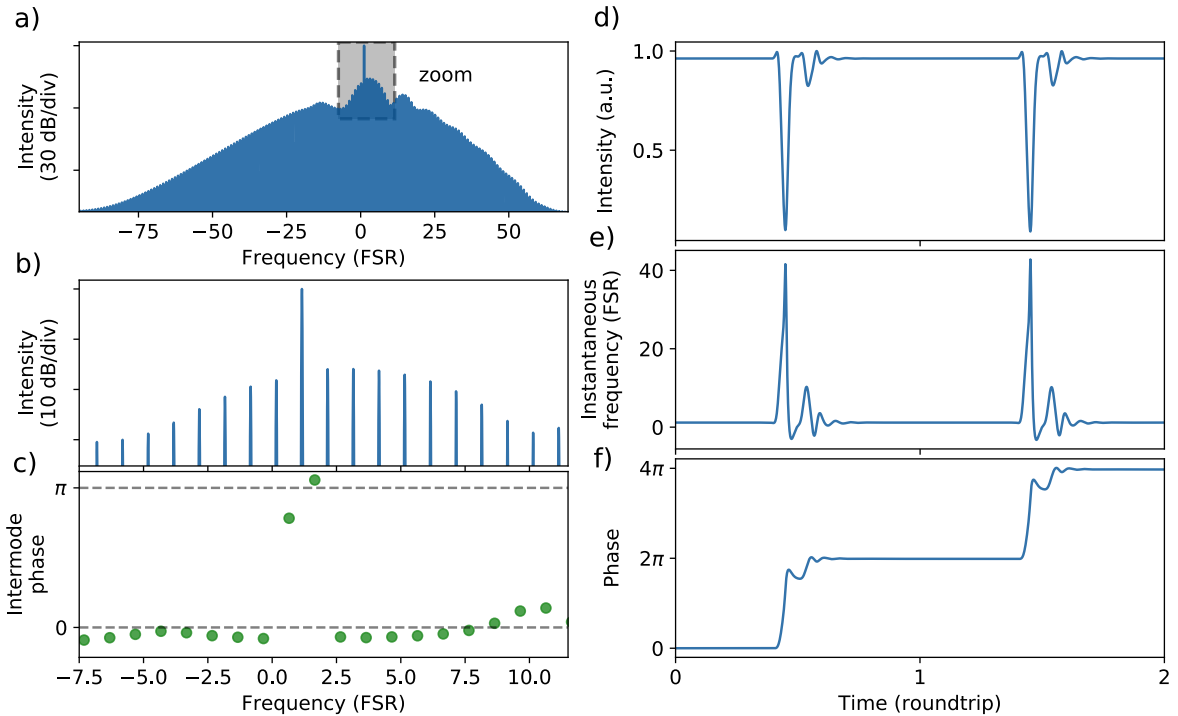


Figure 5: Simulated NBH with $\tilde{\alpha} = 1.25$ and waveguide GVD= 600 fs²/mm. **a)** The intensity spectrum with the shaded region representing the zoomed part of the spectrum shown in **b)**. **c)** Intermodal phases. The **d)** intensity, **e)** instantaneous frequency, and **f)** instantaneous phase in the temporal domain.

One of the NBH states is shown in Fig. 5. It was obtained for $\tilde{\alpha} = 1.25$ and the waveguide GVD= 600 fs²/mm (the total GVD, that includes the gain dispersion accounted for by the LEF, is negative). The spectrum is characterized with a strong single mode surrounded by a broadband smooth spectral envelope. The intermodal phases, which represent the phase differences between the

neighboring modes in the spectrum, are almost flat and identical throughout the spectrum, despite having two offsets equal to π surrounding the strongest mode near the middle of the spectrum. This means that all of the modes belonging to the broadband smooth envelope are in-phase with each other, and the strong mode is exactly π out of phase. In the time domain, this means that the strong mode, which is responsible by the continuous-wave intensity background, interferes destructively with all of the weaker sidemodes. This means that there is a pronounced dark pulse in the waveform, which is surrounded by the otherwise constant intensity (which comes from the strongest mode) – a signature of a NBH dark soliton. Analyzing the instantaneous frequency, one can observe that it changes only within the region of the dark soliton, and is completely constant between the two consecutive solitons. This means that the dark soliton connects two plane waves, which agrees with the CGLE theory of NBHs [28]. Another signature of these states is observed from the instantaneous phase shown in Fig. 5f). At the position of the NBH, there is a steep linear ramp of the phase whose height is exactly equal to 2π – a consequence of the the fact that the strongest mode is anti-phase compared to the rest of the weaker modes in the spectrum.

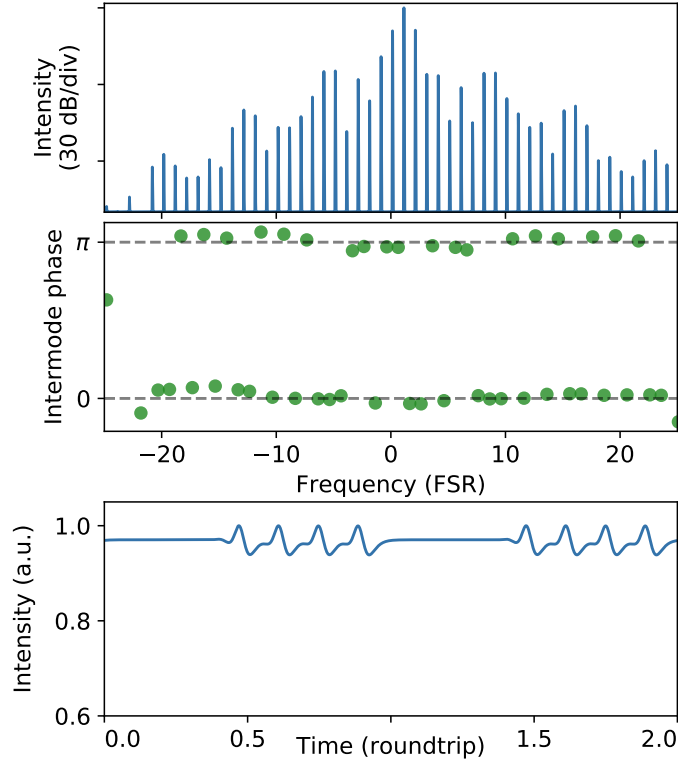


Figure 6: Simulated homoclon state with $\tilde{\alpha} = 1.25$ and waveguide GVD= $-1200 \text{ fs}^2/\text{mm}$.

For completeness, we simulated also a homoclon frequency comb state, depicted in Fig. 6. It is obtained for larger values of negative dispersion, by bringing the laser parameters into the linearly-unstable region of the master equation – akin to what was shown in Fig. 4. In this sense, a stable single-mode laser operation or a NBH state cannot exist for the same value of parameters for which a homoclon state can be obtained. From the Fig. 6, it is seen that the homoclons are fundamentally different from the NBHs, although both represent localized structures in the waveform. The most striking difference is apparent when comparing the intermodal phases, where for a homoclon they

are grouped in two clusters separated by π in seemingly a random way.

Another sign of the solitonic nature of the NBHs is the multistability – a phenomenon where the waveform can be different for the same values of laser parameters, depending on just the starting conditions.

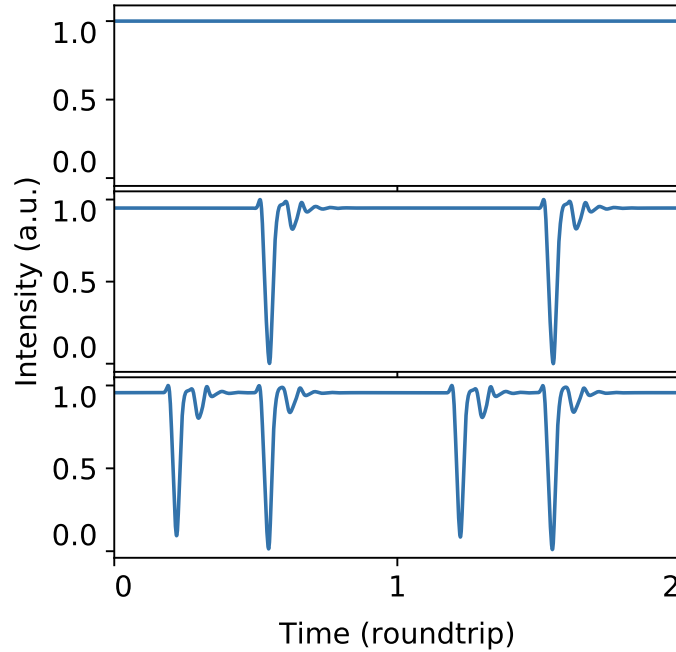


Figure 7: Multistability of the simulated NBH states depending on the starting condition. From top to bottom: single-mode operation, single dark soliton, and two dark solitons per roundtrip.

The results of the simulations that confirm the multistability can be observed in Fig. 7. The coexistence of a stable single-mode solution and a single NBH per roundtrip is seen on the upper two plots. Furthermore, for the same laser parameters, a state which has two NBHs per roundtrip can be seen in the bottom plot.

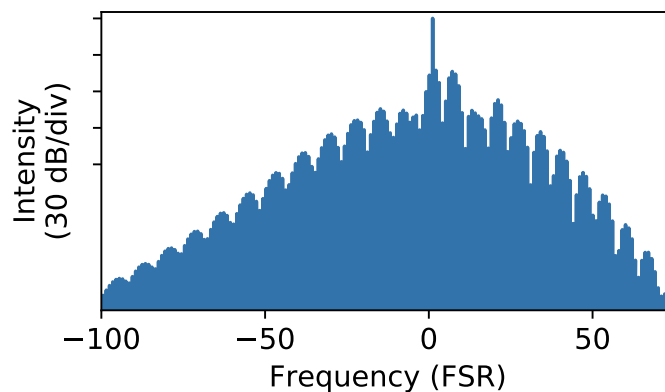


Figure 8: Spectrum of the multisoliton state exhibiting two NBHs per roundtrip. The spectral envelope has a characteristic modulated shape.

The multisoliton state that exhibits two NBHs per roundtrip can be analyzed in closer detail. The optical spectrum is shown on Fig. 8. The spectral envelope becomes modulated and exhibits “spectral holes” at regular intervals – akin to what was previously observed in multisoliton states

from microresonators [30].

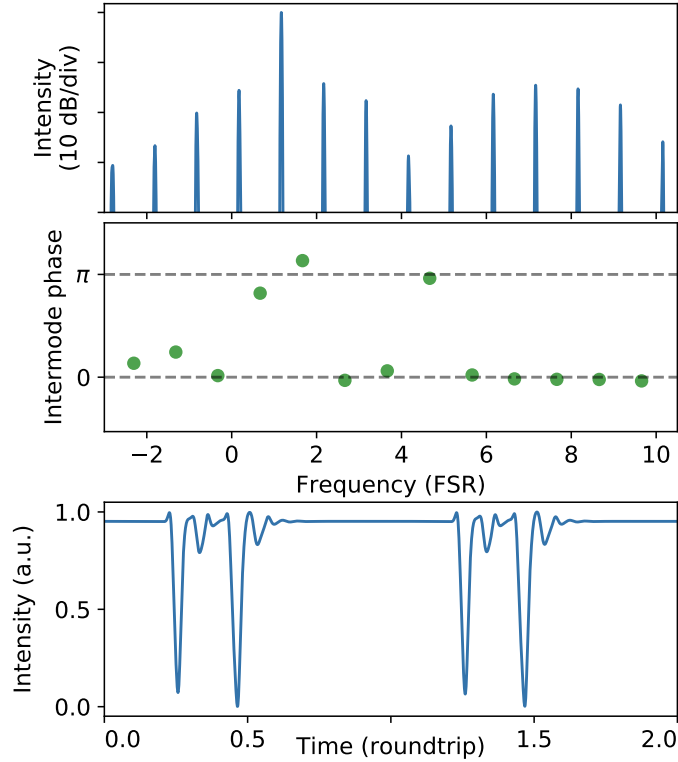


Figure 9: Zoomed part of the spectrum from Fig. 8. The intermodal phases exhibit another π jump between the two spectral smooth lobes, besides the two usual π jumps around the strongest mode. This results in the formation of a second dark soliton (NBH) in the intensity waveform.

Going closer in detail, the zoomed multisoliton spectrum is shown in the top of Fig. 9, where two smooth spectral lobes can be seen. The intermodal phases exhibit another π jump that occurs between these two smooth lobes, besides the usual two π jumps around the strongest mode. Multisoliton states with a larger number of NBHs per roundtrip have also been obtained for similar values of the parameters. In that case, the envelope of the spectrum becomes modulated in an increasingly irregular way, in agreement with observations of multisoliton states in microresonators [30].

3 Task 2 – Device characterization and experimental measurements

Within the Task 2 of this project, we have first designed and fabricated an improved ring laser that employs coupled cavities. We have furthermore characterized the device and built the SWIFTS setup [31] in order to evaluate the coherence of the observed frequency comb states and extract their temporal intensity waveform. We have confirmed our theoretical predictions from Task 1. The results are not published yet.

3.1 Ring QCL device

I will discuss here the ring QCL device that was fabricated within the scope of this project. The device physics and characterization have been discussed and published in Ref. [32]. Instead of fabricating a simple ring resonator, like it was done in Ref. [13], we have opted for an improved design, as can be seen in Fig. 10.

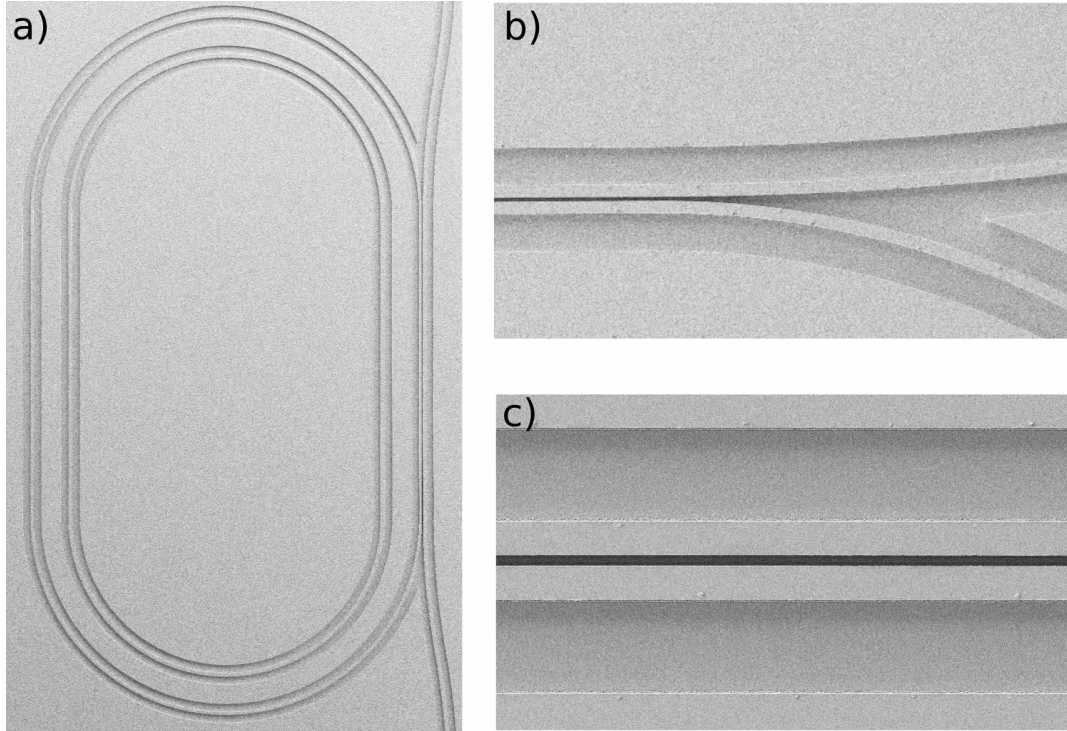


Figure 10: **a)** Fabricated ring QCL with an active coupler waveguide for efficient light extraction. **b)** Zoomed section where the coupler waveguide approaches the ring cavity. **c)** Zoomed straight coupling section of the ring and the coupler. The waveguide's width of both the ring and the coupler is $10\ \mu\text{m}$ and the gap between them is around $2\ \mu\text{m}$.

Having an ideal ring resonator, as is sketched in Fig. 1 implies one large practical problem – there is no way how to deliberately extract the light that is propagating inside the cavity. The only way how to measure the light is by random inefficient scattering, and even then the extracted light power is in the range of microwatts [13]. This level of power is severely limiting device characterization and is not enough to characterize the frequency comb regime by employing the SWIFTS technique. For this reason, we have fabricated our ring resonators in a shape of a racetrack, which has two straight sections that connect semi-circle sections. The straight section is brought into the vicinity of another straight waveguide so that they become coupled (Fig. 10). In this way, the light that circulates inside the ring resonator can be outcoupled into the coupler waveguide and then be emitted at much higher power levels compared to an ideal ring device. The ring and the coupler waveguide are biased separately. This reason for this is twofold. First of all, separate electrical bias allows different optical gain or absorption inside the two coupled cavities (the coupler waveguide is too short to allow lasing on its own) thus enabling to tune their quality factor. Furthermore, changing the bias induces a change of the temperature which changes the refractive index of the material. In this way, by providing a separate electrical bias, we allow to tune the refractive index of the ring and of the coupler waveguide separately, which determines the coupling coeffi-

cient between the two cavities. This has allowed to access undercoupled, critically-coupled, and overcoupled regime with the same device. We show that one device, depending on its operating point, can act as a tunable filter, a nonlinear frequency converter, or a frequency comb generator. These concepts extend to the integration of multiple active resonators and waveguides in arbitrary configurations, thus allowing the implementation of purpose-specific mid-infrared active photonic integrated circuits for spectroscopy, communications, and microwave generation [32].

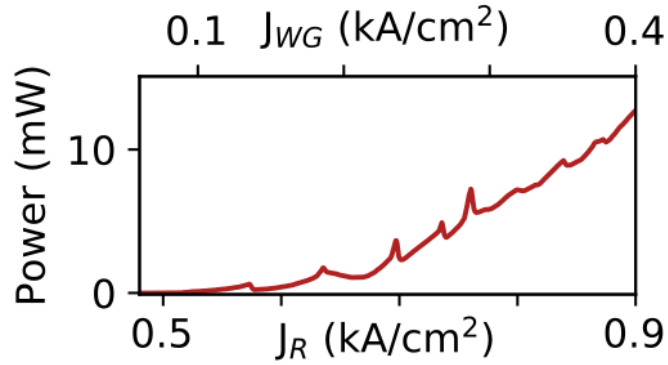


Figure 11: Measured light-current (LI) characteristic of the ring QCL device. We tune both the current of the ring (J_R) and the waveguide coupler (J_{WG}).

The measured light-current (LI) characteristic of the ring QCL is shown in Fig. 11. We tune the currents of both the ring and the waveguide coupler in order to remain near the optimal coupling regime for power extraction. This allows the device to emit more than 10 mW of power, which is two orders of magnitude larger than the ideal ring QCL fabricated from the same growth material [13], and comparable to the emission from a Fabry-Perot ridge laser whose length is similar to the ring circumference (around 7 mm) [32].

3.2 Frequency comb and dark soliton characterization

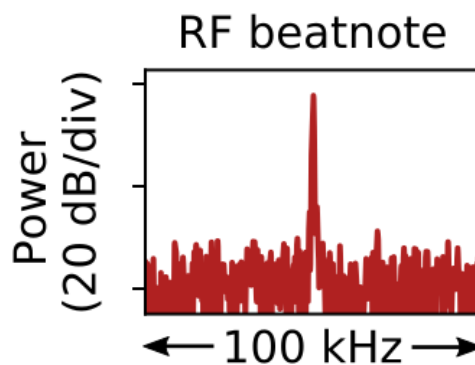


Figure 12: Measured optical beatnote of the ring QCL. The narrow profile indicates frequency comb operation.

The first strong evidence that indicates frequency comb operation of the laser is its optical beatnote. The neighboring modes in a multimode spectrum beat together and create a signal at their difference frequency, due to the highly nonlinear active medium of the laser. If the difference frequency of all of the neighboring modes is identical and equal to the repetition frequency, as is the

case in a frequency comb, then all of the individual beating signals add together to produce a collective beatnote with a narrow profile. However, if the laser spectrum is not completely equidistant, the collective beatnote will be weaker and with a broad profile.

We have measured the optical beatnote by focusing the laser light onto a quantum well infrared photodiode, and the data can be seen in Fig. 12. The strong beatnote with a narrow profile strongly suggest that the laser is operating in a frequency comb regime.

In order to evaluate the intensity waveform of the comb, we employ a very elegant experimental technique called SWIFTS [31]. In essence, it relies on the measurement of two interferograms employing the Fourier-transform infrared (FTIR) spectrometer – one DC interferogram that yields the intensity spectrum, and a second one at the repetition frequency, which allows to obtain the complex beatnote spectrum. With this knowledge, it is possible to extract the value of the intermodal phases, and together with the modal amplitudes, we can then reconstruct the laser field in the time domain.

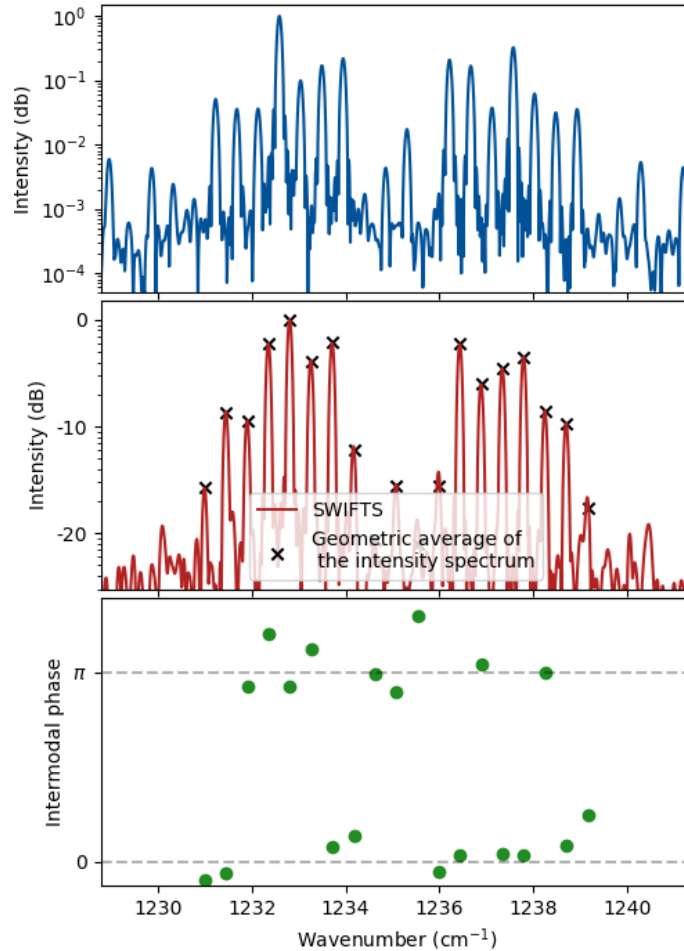


Figure 13: Experimental characterization of a homoclon frequency comb state. The intensity spectra are plotted on the top. The middle plot depicts the beatnote spectrum obtained from SWIFTS. If the state is perfectly coherent, as it should be for a frequency comb, the beatnote spectrum amplitudes are equal to the geometric average of the neighboring amplitudes of the intensity spectrum, which can be seen from the plot. The intermodal phases (bottom) are grouped in two clusters separated by π .

We initially confirmed the existence of homoclon states in the newly-processed ring QCLs with coupler waveguides. These states should be attained for a larger negative GVD, where the single-

mode laser operation is destabilized [13]. The results can be seen in Fig. 13. The coherence of the state is proven with the SWIFTS technique by comparing the SWIFTS beatnote spectrum with the geometric average of neighboring modes in the intensity spectrum – if they overlap, the laser operates in a frequency comb state. The intermodal phases can be seen to group in two clusters separated by π , as was obtained in the simulation displayed in Fig. 6.

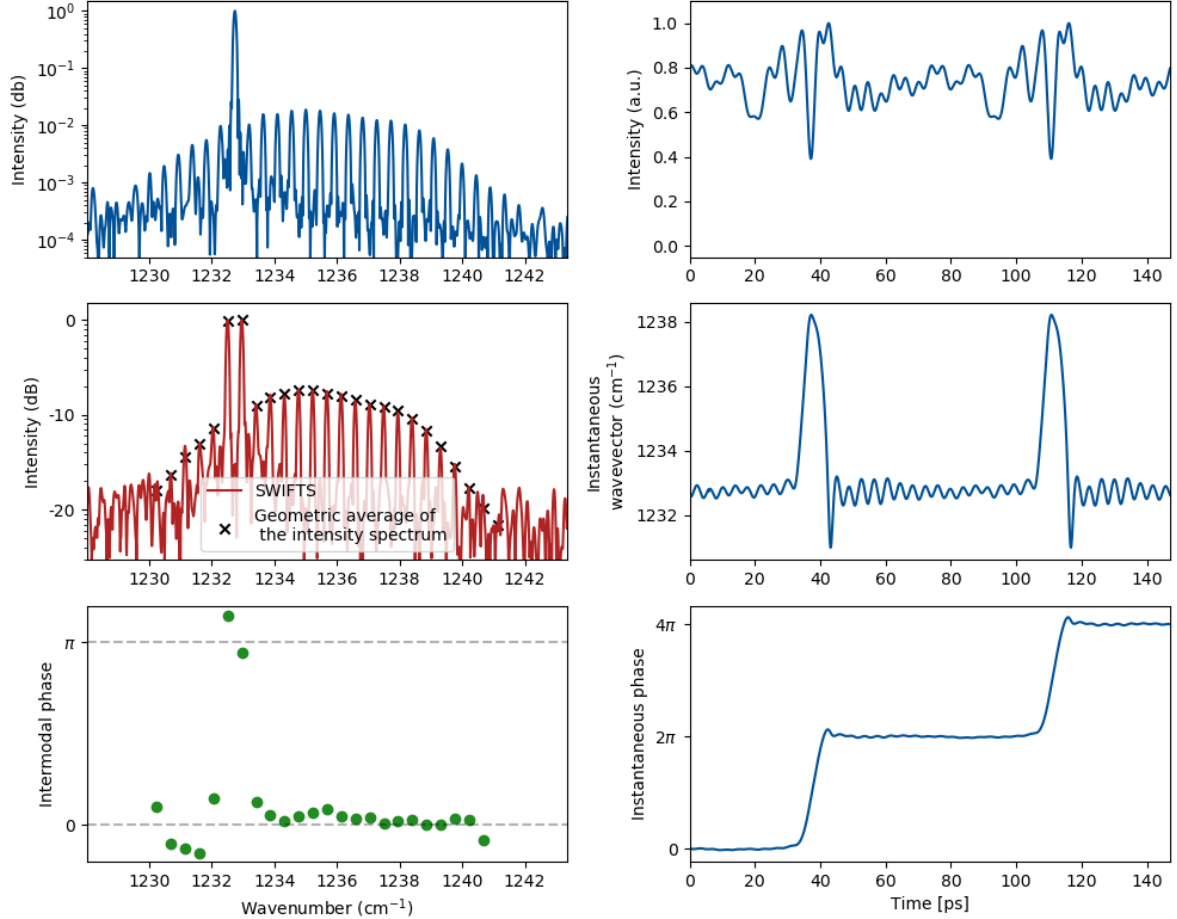


Figure 14: Experimental characterization of a dark soliton state. The left column shows from top to bottom the intensity spectrum, the SWIFTS spectrum, and the intermodal phases. The identical π jump in the intermodal phases can be observed around the strongest mode in the spectrum as is shown in Fig. 5 for a simulated dark soliton. The right column shows the reconstructed temporal intensity waveform, the instantaneous wavenumber, and the phase. The instantaneous wavenumber changes only within the dark pulse (NBH) and remains constant elsewhere. The phase exhibits a linear ramp of 2π across the dark soliton.

Furthermore, by changing the electrical bias of the identical device, we were able to experimentally confirm also the existence of predicted dark solitons in the form of NBHs (Fig. 14). The intensity spectrum consisting of a strong mode surrounded by a single smooth envelope is plotted in the top of the left column, matching the zoomed portion of the simulated spectrum in Fig. 5b). In the experiments, we are limited by the detector and the dynamic range barely exceeds three orders of magnitude, in sharp contrast to the simulations, where the range is much larger. For this reason we compare only the zoomed portion of the simulated spectrum. Furthermore, from the SWIFTS spectrum, one can infer that the observed state is fully coherent and is indeed a frequency comb. The intermodal phases are characterized by the π jumps around the strongest mode, and

are nearly constant for the sidemodes. In temporal domain (right column), one can observe a dark pulse appearing once per roundtrip. The amplitude contrast of the dark pulse is not as large as in the simulations, which can be explained by the limited bandwidth imposed by the dynamic range of the detector, and phase errors. The instantaneous wavevector, which is proportional to the instantaneous frequency, changes swiftly within the region of the dark pulse, and remains constant elsewhere, indicating that the dark pulse is surrounded by a plane wave which contains a single frequency – that of the strongest mode. This is in agreement with the simulated waveform from Fig. 5 and also with the theory of NBHs in the CGLE formalism – furthermore corroborating the soliton nature of the state. Finally, the temporal phase profile again agrees with our predictions – it exhibits a sharp ramp of 2π across the soliton. The cumulative evidence and agreement with the simulation and experiments depicted in Figs. 5 and 14 proves that we obtain a dark soliton in the form of a NBH – thus making the ring QCL device the first integrated electrically-driven platform for soliton generation.

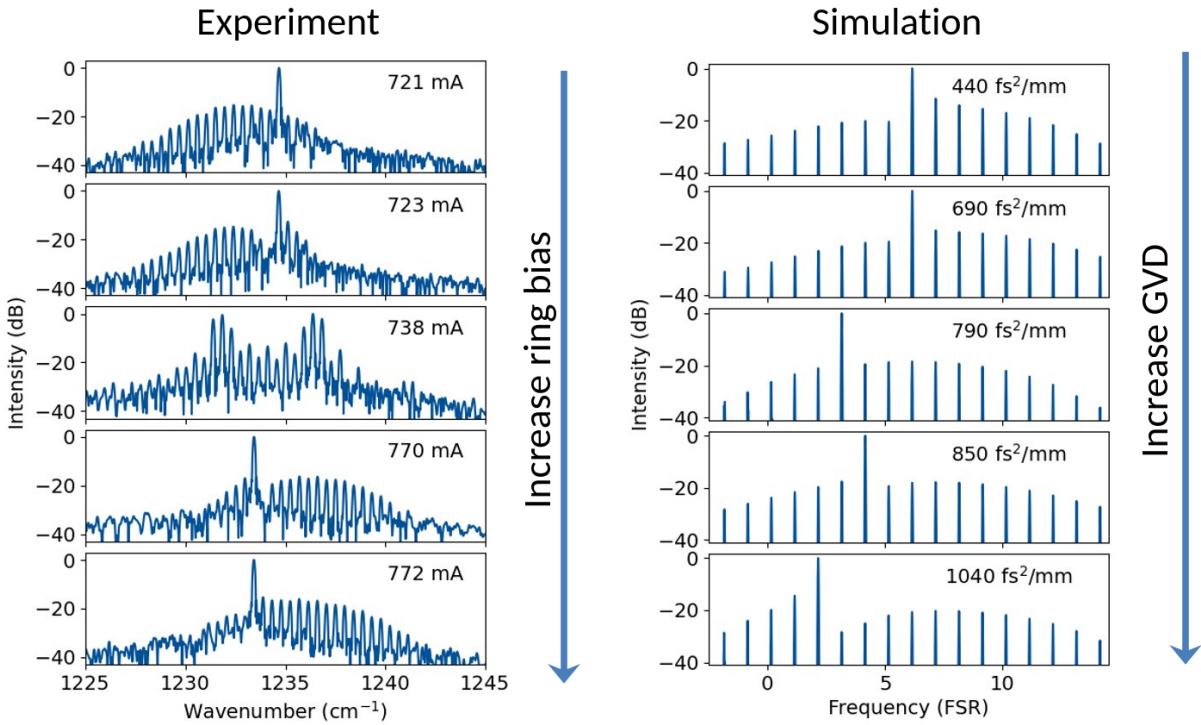


Figure 15: Coherent control of the dark soliton states in the experiment (left column) and in the simulation (right column). By changing the bias of the ring QCL in the experiments, we are able to influence the solitonic state and change the position of the smooth spectral envelope relative to the position of the strong mode. In the simulations, a similar effect is obtained by changing the waveguide GVD.

In the experiments, the only control knobs we possess are the bias currents of the ring laser and of the coupler waveguide. Due to the improved QCL cavity device design [32], these two currents provide a powerful control parameter. Fig. 15 displays on the left the evolution of the experimentally measured spectra as we tune the bias of the ring QCL. We can observe that the solitonic smooth spectral envelope moves relative to the position of the strong mode – from red to the blue side. As we change the current of the laser, we influence many parameters, some of which are the refractive index and the coupling coefficient between the ring and the waveguide. This strongly modifies the GVD of the mode, which should have a gross impact on the laser state. We confirm this by

numerical simulations, where we can control the value of the waveguide GVD, as is displayed on the right side of Fig. 15. The spectral envelope is influenced heavily by the value of the GVD, and also shifts relative to the strongest mode. Further theoretical studies are necessary to determine the exact influence of the dispersion on the NBH dark solitons. This knowledge could then be applied to design ring laser devices with specific-tailored GVD in order to unlock the full potential of dark soliton states.

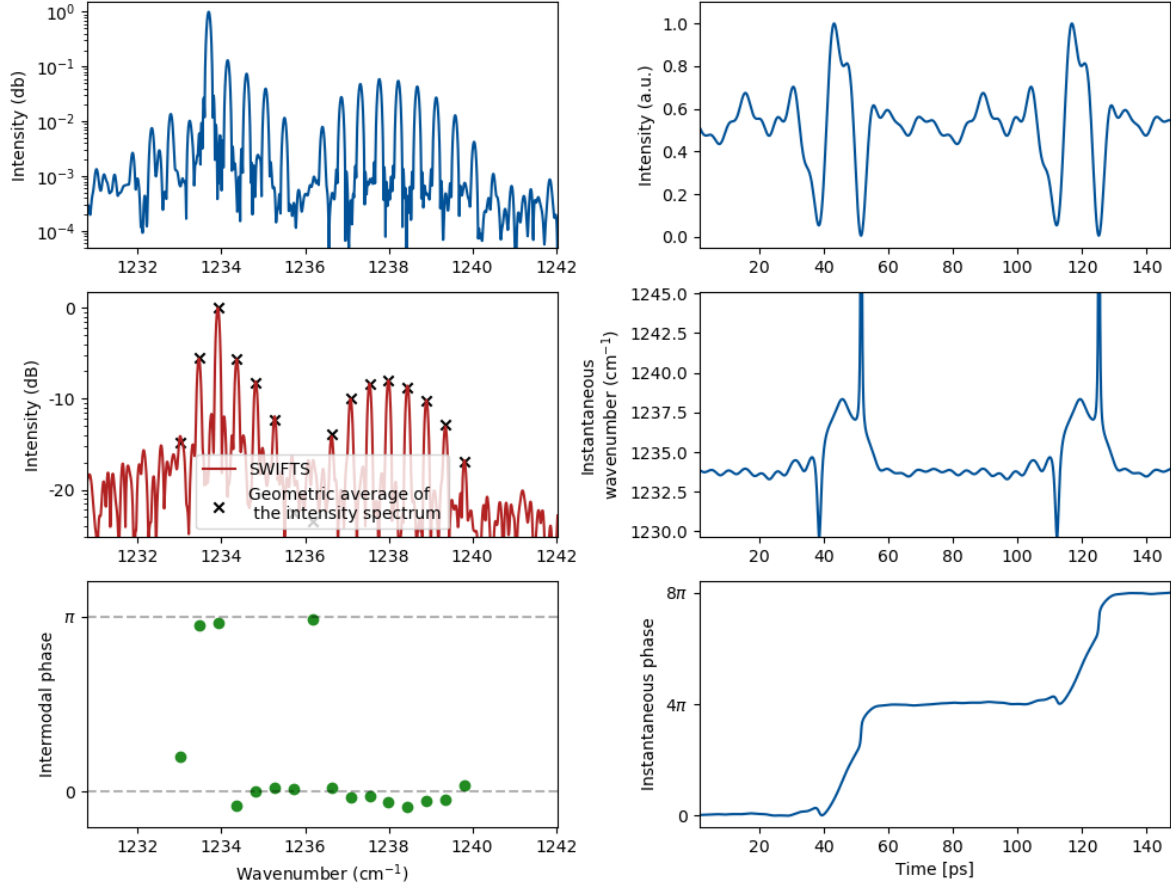


Figure 16: Characterisation of a multisoliton state in a ring QCL. The figure is organized as Fig. 5.

Lastly, we demonstrate also a multisoliton state in our ring QCL, as is seen in Fig. 16. Again, excellent agreement can be observed with the simulations (Fig. 9). The spectrum consists of two separated smooth envelopes, which is a consequence of two NBHs existing within one roundtrip. In the spectral domain, the intermodal phases show one more π phase jump exactly between the two envelopes, besides the usual two jumps around the strongest mode. The instantaneous wavenumber has two sharp peaks, each happening within the region of the corresponding dark pulse. Furthermore, these peaks have opposite directions due to the fact that there is a π phase jump between the two spectral envelopes. The blue-sided envelope is also wider than the red-sided one, which explains why the corresponding peak of the instantaneous wavenumber is larger. The instantaneous wavenumber is again constant in the remaining part of the roundtrip. The temporal phase changes a total amount of 4π over the two dark solitons, in contrast to the case of only one soliton per roundtrip, where the phase change was only 2π .

4 Conclusion and impact of the conducted research

During my research visit at the Harvard University, within the scope of the Marshall Plan Scholarship, we have achieved the bulk of the proposed investigation. First of all, the theoretical model of the laser was improved by considering the linewidth enhancement factor (LEF), which is one of the most important parameters of the lasers and has a huge impact on the dynamic evolution of the multimode emission (results are published in my doctoral thesis). The state-of-the-art full Maxwell-Bloch system of equations was furthermore greatly simplified in order to obtain a single master equation that governs the laser dynamics and that includes all of the important mechanisms. The cumulative efforts in developing a realistic theoretical description of laser physics resulted in a highly sophisticated numerical model capable of simulating a plethora of laser multimode regimes.

The knowledge of the master equation allows to tame the complexity of the system and gain intuitive insights – which led us to describe the QCL ring system within the formalism of the famous complex Ginzburg-Landau equation (CGLE). By doing this, we were able to explain the single-mode instabilities that were observed in these lasers. Within this project, we build upon our previous insights and go beyond the linear regime in order to predict the emission of dark solitons in ring QCLs in the form of Nozaki-Bekki holes that are known from the CGLE theory, but haven't been observed so far in monolithic laser systems. For this reason we opted to deal only with ring laser cavities within this project. Subsequently, we demonstrate the existence of predicted dark solitons in ring QCLs – both in the simulations based on the master equation and also in experiments. These results are in preparation to be submitted.

The impact of these findings is reflected in the discovery of a completely novel type of a frequency comb. Optical solitons have previously been known mostly in microresonator cavities and optical fibers, which are both passive media that require external optical injection. This significantly increases the complexity and dimensions of the system, which prohibits any use outside of laboratory conditions. Our findings were observed in a monotonically-integrated and electrically-driven semiconductor laser, which can fit on a single chip. Besides this practical viewpoint, our findings open a new chapter in photonics by demonstrating solitons in a medium that was thought to not be able to support their existence according to traditional theory – thus begging for a theory revision and adding more fuel to the everlasting search for new states of light.

5 References

- [1] S. A. Diddams, K. Vahala, and T. Udem. “Optical frequency combs: Coherently uniting the electromagnetic spectrum”. *Science* **369**, 6501 (July 2020). doi: [10.1126/science.aay3676](https://doi.org/10.1126/science.aay3676).
- [2] T. Udem, R. Holzwarth, and T. W. Hänsch. “Optical frequency metrology”. *Nature* **416** (2002) pp. 233–237. doi: [10.1038/416233a](https://doi.org/10.1038/416233a).
- [3] R. Holzwarth, T. Udem, T. W. Hänsch, J. C. Knight, W. J. Wadsworth, and P. S. J. Russell. “Optical Frequency Synthesizer for Precision Spectroscopy”. *Physical Review Letters* **85** (2000) pp. 2264–2267. doi: [10.1103/physrevlett.85.2264](https://doi.org/10.1103/physrevlett.85.2264).
- [4] B. Bernhardt, A. Ozawa, P. Jacquet, M. Jacquety, Y. Kobayashi, T. Udem, R. Holzwarth, G. Guelachvili, T. W. Hänsch, and N. Picqué. “Cavity-enhanced dual-comb spectroscopy”. *Nature Photonics* **4** (2009) pp. 55–57. doi: [10.1038/nphoton.2009.217](https://doi.org/10.1038/nphoton.2009.217).
- [5] J. Faist, F. Capasso, D. L. Sivco, C. Sirtori, A. L. Hutchinson, and A. Y. Cho. “Quantum Cascade Laser”. *Science* **264** (1994) pp. 553–556. doi: [10.1126/science.264.5158.553](https://doi.org/10.1126/science.264.5158.553).
- [6] J. Faist. *Quantum Cascade Lasers*. Oxford, UK: Oxford University Press, 2013.
- [7] N. Opačak, S. D. Cin, J. Hillbrand, and B. Schwarz. “Frequency Comb Generation by Bloch Gain Induced Giant Kerr Nonlinearity”. *Physical Review Letters* **127**, 9 (Aug. 2021). doi: [10.1103/physrevlett.127.093902](https://doi.org/10.1103/physrevlett.127.093902).
- [8] A. Hugi, G. Villares, S. Blaser, H. C. Liu, and J. Faist. “Mid-infrared frequency comb based on a quantum cascade laser”. *Nature* **492** (2012) pp. 229–233. doi: [10.1038/nature11620](https://doi.org/10.1038/nature11620).
- [9] N. Opačak and B. Schwarz. “Theory of frequency modulated combs in lasers with spatial hole burning, dispersion and Kerr”. *Physical Review Letters* **123** (2019) p. 243902. [web link](#).
- [10] J. Hillbrand, A. M. Andrews, H. Detz, G. Strasser, and B. Schwarz. “Coherent injection locking of quantum cascade laser frequency combs”. *arXiv preprint arXiv:1808.06636*, (2018). [web link](#).
- [11] M. Beiser, N. Opačak, J. Hillbrand, G. Strasser, and B. Schwarz. “Engineering the spectral bandwidth of quantum cascade laser frequency combs”. *Optics Letters* **46** (July 2021) p. 3416. doi: [10.1364/ol.424164](https://doi.org/10.1364/ol.424164).
- [12] J. Hillbrand, N. Opačak, M. Piccardo, H. Schneider, G. Strasser, F. Capasso, and B. Schwarz. “Mode-locked short pulses from an 8 μm wavelength semiconductor laser”. *Nature Communications* **11**, 1 (Nov. 2020). doi: [10.1038/s41467-020-19592-1](https://doi.org/10.1038/s41467-020-19592-1).
- [13] M. Piccardo, B. Schwarz, D. Kazakov, M. Beiser, N. Opačak, Y. Wang, S. Jha, J. Hillbrand, M. Tamagnone, W. T. Chen, A. Y. Zhu, L. L. Columbo, A. Belyanin, and F. Capasso. “Frequency combs induced by phase turbulence”. *Nature* **582** (June 2020) pp. 360–364. doi: [10.1038/s41586-020-2386-6](https://doi.org/10.1038/s41586-020-2386-6).
- [14] D. Kazakov, N. Opačak, M. Beiser, A. Belyanin, B. Schwarz, M. Piccardo, and F. Capasso. “Defect-engineered ring laser harmonic frequency combs”. *Optica*, (Aug. 2021). doi: [10.1364/optica.430896](https://doi.org/10.1364/optica.430896).

- [15] B. Meng, M. Singleton, M. Shahmohammadi, F. Kapsalidis, R. Wang, M. Beck, and J. Faist. “Mid-infrared frequency comb from a ring quantum cascade laser”. *Optica* **7** (2020) p. 162. doi: [10.1364/optica.377755](https://doi.org/10.1364/optica.377755).
- [16] T. S. Mansuripur, C. Vernet, P. Chevalier, G. Aoust, B. Schwarz, F. Xie, C. Caneau, K. Lascola, C. en Zah, D. P. Caffey, T. Day, L. J. Missaggia, M. K. Connors, C. A. Wang, A. Belyanin, and F. Capasso. “Single-mode instability in standing-wave lasers: The quantum cascade laser as a self-pumped parametric oscillator”. *Physical Review A* **94**, 6 (2016). doi: [10.1103/physreva.94.063807](https://doi.org/10.1103/physreva.94.063807).
- [17] N. Opačak. “The origin of frequency combs in free-running quantum cascade lasers”. en. PhD thesis. 2022. doi: [10.34726/HSS.2022.103442](https://doi.org/10.34726/HSS.2022.103442).
- [18] R. W. Boyd. *Nonlinear optics*. Academic press, 2003.
- [19] I. Walmsley, L. Waxer, and C. Dorrer. “The role of dispersion in ultrafast optics”. *Review of Scientific Instruments* **72** (Jan. 2001) pp. 1–29. doi: [10.1063/1.1330575](https://doi.org/10.1063/1.1330575).
- [20] C. H. Henry. “Theory of the linewidth of semiconductor lasers”. *IEEE J. Quantum Electron.* **18** (1982) pp. 259–264. doi: [10.1109/JQE.1982.1071522](https://doi.org/10.1109/JQE.1982.1071522).
- [21] A. Yariv. *Quantum Electronics*. Third. New York, USA: John Wiley & Sons, 1989.
- [22] G. P. Agrawal. “Population pulsations and nondegenerate four-wave mixing in semiconductor lasers and amplifiers”. *Journal of the Optical Society of America B* **5** (1988) p. 147. doi: [10.1364/josab.5.000147](https://doi.org/10.1364/josab.5.000147).
- [23] L. Columbo, M. Piccardo, F. Prati, L. Lugiato, M. Brambilla, A. Gatti, C. Silvestri, M. Gioannini, N. Opačak, B. Schwarz, and F. Capasso. “Unifying Frequency Combs in Active and Passive Cavities: Temporal Solitons in Externally Driven Ring Lasers”. *Physical Review Letters* **126**, 17 (Apr. 2021). doi: [10.1103/physrevlett.126.173903](https://doi.org/10.1103/physrevlett.126.173903).
- [24] N. Opačak, F. Pilat, D. Kazakov, S. D. Cin, G. Ramer, B. Lendl, F. Capasso, and B. Schwarz. “Spectrally resolved linewidth enhancement factor of a semiconductor frequency comb”. *Optica* **8** (Sept. 2021) p. 1227. doi: [10.1364/optica.428096](https://doi.org/10.1364/optica.428096).
- [25] M. Jaidl, N. Opačak, M. A. Kainz, S. Schönhuber, D. Theiner, B. Limbacher, M. Beiser, M. Giparakis, A. M. Andrews, G. Strasser, B. Schwarz, J. Darmo, and K. Unterrainer. “Comb operation in terahertz quantum cascade ring lasers”. *Optica* **8** (May 2021) p. 780. doi: [10.1364/optica.420674](https://doi.org/10.1364/optica.420674).
- [26] M. Jaidl, N. Opačak, M. A. Kainz, D. Theiner, B. Limbacher, M. Beiser, M. Giparakis, A. M. Andrews, G. Strasser, B. Schwarz, J. Darmo, and K. Unterrainer. “Silicon integrated terahertz quantum cascade ring laser frequency comb”. *Applied Physics Letters* **120** (2022) p. 091106. doi: [10.1063/5.0078749](https://doi.org/10.1063/5.0078749).
- [27] “XXIX. An experimental investigation of the circumstances which determine whether the motion of water shall be direct or sinuous, and of the law of resistance in parallel channels”. *Philosophical Transactions of the Royal Society of London* **174** (1883) pp. 935–982. doi: [10.1098/rstl.1883.0029](https://doi.org/10.1098/rstl.1883.0029).
- [28] I. S. Aranson and L. Kramer. “The world of the complex Ginzburg-Landau equation”. *Reviews of Modern Physics* **74** (2002) pp. 99–143. doi: [10.1103/revmodphys.74.99](https://doi.org/10.1103/revmodphys.74.99).

- [29] J. Lega. “Traveling hole solutions of the complex Ginzburg–Landau equation: a review”. *Physica D: Nonlinear Phenomena* **152-153** (2001) pp. 269–287. doi: [10.1016/s0167-2789\(01\)00174-9](https://doi.org/10.1016/s0167-2789(01)00174-9).
- [30] T. J. Kippenberg, A. L. Gaeta, M. Lipson, and M. L. Gorodetsky. “Dissipative Kerr solitons in optical microresonators”. *Science* **361**, 6402 (2018). doi: [10.1126/science.aan8083](https://doi.org/10.1126/science.aan8083).
- [31] D. Burghoff, Y. Yang, D. J. Hayton, J.-R. Gao, J. L. Reno, and Q. Hu. “Evaluating the coherence and time-domain profile of quantum cascade laser frequency combs”. *Optics Express* **23** (2015) p. 1190. doi: [10.1364/oe.23.001190](https://doi.org/10.1364/oe.23.001190).
- [32] D. Kazakov, T. P. Letsou, M. Beiser, Y. Zhi, N. Opačak, M. Piccardo, B. Schwarz, and F. Capasso. *Semiconductor ring laser frequency combs with active directional couplers*. 2022. doi: [10.48550/ARXIV.2206.03379](https://doi.org/10.48550/ARXIV.2206.03379).